Inclusive Dijet Production at HERA: Direct Photon Cross Sections in Next-To-Leading Order QCD

M. Klasen, G. Kramer
II. Institut für Theoretische Physik[*]
Universität Hamburg
D - 22761 Hamburg, Germany

Abstract

We have calculated inclusive two-jet cross sections in next-to-leading order QCD for direct photoproduction in low Q^2 ep collisions at HERA. Infrared and collinear singularities in real and virtual contributions are cancelled with the phase space slicing method. Analytical formulas for the different contributions giving the dependence on the slicing parameter are presented. Various one- and two-jet distributions have been computed demonstrating the flexibility of the method.

1 Introduction

Electron-proton scattering at HERA proceeds dominantly through the exchange of photons with very small virtuality ($Q^2 \simeq 0$). An important fraction of the γp collisions contains high transverse momentum (E_T) processes. The presence of this hard momentum scale allows the application of perturbative QCD to predict cross sections for the production of two or more high-E_T jets.

In lowest order (LO) QCD, the hard scattering processes can be classified in two types [1, 2]. In the so-called direct process, the photon interacts in a point-like fashion with the quark which appears either in the QCD Compton scattering $\gamma q \to gq$ or the photon-gluon fusion process $\gamma g \to q\bar{q}$. In the resolved process, the photon acts as a source of partons, which can scatter with the partons coming out of the proton. These two processes give two distinctly different types of high-E_T event topologies. The point-like interaction results in events with a characteristic (2+1)-jet structure, i.e. two high-E_T jets and one jet of low E_T fragments of the proton. The resolved photon events have a characteristic (2+2)-jet structure, since in addition to the two high-E_T jets and the low-E_T proton remnant, fragments coming from the photon will produce a second low-E_T jet. While in the (2+1)-jet events the total photon energy contributes to the hard scattering process, only a fraction participates in the (2+2)-jet events.

Several methods for detecting the photon remnant jet have been proposed and tested in Monte Carlo simulations, generally using a cut on the energy in the photon direction or other kinematical variables [3, 4]. Using an E_T cluster algorithm, the ZEUS collaboration was actually able to select events with two high-E_T jets and a third cluster in the approximate direction of the electron (photon) beam [5]. They studied the properties of the photon remnant jet and found them to agree with expectations. This shows that photoproduction events with a photon remnant jet can be identified experimentally.

Unfortunately, this does not lead to a separation of the direct and resolved processes, because their characterization described above is only valid in LO QCD. In NLO, the direct cross section may also have contributions with a photon remnant jet. Therefore its detection does not uniquely separate the resolved cross section. In a complete NLO calculation the direct contributions with a photon remnant jet could be isolated, so that the remaining contributions could be compared with the (2+1)-jet configuration. Of course, in this case the selection procedure in the experimental analysis and in the theoretical calculation must match. To make further progress in this direction, a complete NLO calculation of the direct cross section is needed which is flexible enough to incorporate the possible selection criteria for the high-E_T jets and the low-E_T remnant jets. NLO calculations of direct photoproduction have been done in the past for inclusive single hadron [6], inclusive single jet [7, 8, 9], and for inclusive dijet [7, 10] cross sections. Most of these results are applicable only for special observables in inclusive single jet and dijet production.

The leading order calculation of the direct component involves only two subprocesses: $\gamma q \to gq$ and $\gamma g \to q\bar{q}$. By including terms up to $\mathrm{O}(\alpha\alpha_s^2)$, new contributions arise. These are the one-loop contributions to $\gamma q \to gq$ and $\gamma g \to q\bar{q}$ and the three-body subprocesses $\gamma q \to qgg$, $\gamma q \to qq\bar{q}$, $\gamma q \to qq'\bar{q}'$, and $\gamma g \to gq\bar{q}$. Besides the ultraviolet singularities in the one-loop contributions, which can be removed by renormalization, additional infrared and

collinear singularities occur. They are extracted with the dimensional regularization method. It is well known that for suitably defined inclusive observables the infrared singularities in the one-loop contributions will cancel against those in the three-body tree diagrams. The collinear singularities from initial state radiation and $q\bar{q}$ production at the photon leg can be factorized and absorbed in the respective parton distribution functions. The hard collinear singularities from final state radiation will cancel against the corresponding singularities in the one-loop graphs. To achieve this technically and to maintain also the necessary flexibility for new choices of observables, jet definitions, and experimental cuts, we use the so-called phase space slicing method. We introduce an invariant mass cut-off y, which allows us to separate the phase space regions containing the singularities. If y is chosen sufficiently small, the integration over the soft and collinear regions can be performed analytically in a straightforward way. Then y is just a technical cut which needs not be connected with the experimental jet definition. Of course, the suitably defined inclusive one- and two-jet cross sections must be independent of y. Our method is very similar to that of Baer et al. [7] who used two distinct cut-off parameters for soft and collinear singularities. The phase space slicing method with invariant mass cut-off has been used for many processes. The calculation for photoproduction proceeds along the same line as the calculation of higher order QCD corrections for multijet cross sections in deep inelastic ep scattering first performed by Graudenz [11].

The plan of the paper is as follows: In section 2 we review the LO calculations and fix our notation. The techniques to perform the NLO calculations are explained in section 3. In section 4 we present some results for inclusive one- and two-jet cross sections in order to demonstrate the flexibility of our method. Section 5 contains a summary of our conclusions. In several appendices we provide our analytically calculated results needed for the Monte Carlo computations.

2 Leading Order Cross Sections

2.1 Photon Spectrum

The cross sections we have computed are essentially for kinematical conditions as in the HERA experiments. There, electrons of $E_e = 26.7$ GeV produce photons with small virtuality $Q^2 = -q^2 \simeq 0$, which then collide with a proton beam of energy $E_p = 820$ GeV. $q = p_e - p'_e$ is the momentum transfer of the electron to the photon. The spectrum of the virtual photons is approximated by the Weizsäcker-Williams formula

$$x_a F_{\gamma/e}(x_a) = \frac{\alpha}{2\pi}(1 + (1 - x_a)^2) \ln\left(\frac{Q_{\max}^2(1 - x_a)}{m_e^2 \, x_a^2}\right), \tag{1}$$

where m_e is the electron mass and $x_a = \frac{pq}{pp_e} \simeq E_\gamma/E_e$ is the fraction of the initial electron energy transferred to the photon. p is the four momentum of the incoming proton. In the equivalent photon approximation, the cross section for the process $ep \to e'X$ with arbitrary final state X is then given by the convolution

$$d\sigma(ep \to e'X) = \int_{x_{a,\min}}^1 dx_a F_{\gamma/e}(x_a) d\sigma(\gamma p \to X), \tag{2}$$

where $d\sigma(\gamma p \to X)$ denotes the cross section for $\gamma p \to X$ with real photons of energy $E_\gamma = x_a E_e$.

2.2 Jet Cross Sections in LO

In leading order, the differential cross section for two-jet production takes a very simple form. The partonic subprocesses are $\gamma q \to gq$ and $\gamma g \to q\bar{q}$, which we denote generically by $\gamma b \to p_1 p_2$. b is the parton emitted from the proton with momentum $p_0 = x_b p$. Its distribution function in the proton $F_{b/p}(x_b, M_b^2)$ depends on the momentum fraction x_b and the factorization scale M_b. The final state partons have momenta p_1 and p_2, which can be expressed by their transverse momentum E_T and their rapidities η_1 and η_2. The convention is that the z direction is parallel to the proton beam as used in the experimental analysis. From energy and momentum conservation one obtains

$$x_a = \frac{E_T}{2E_e}\left(e^{-\eta_1} + e^{-\eta_2}\right), \tag{3}$$

$$x_b = \frac{E_T}{2E_p}\left(e^{\eta_1} + e^{\eta_2}\right). \tag{4}$$

Thus, the kinematical variables of the two jets are related to the scaling variables x_a and x_b. For example, the rapidity η_2 of the second jet is kinematically fixed by E_T, η_1, and the photon fraction x_a through the relation

$$\eta_2 = -\ln\left(\frac{2x_a E_e}{E_T} - e^{-\eta_1}\right). \tag{5}$$

In the HERA experiments, x_a is restricted to a fixed interval $x_{a,\min} \leq x_a \leq x_{a,\max} < 1$. We shall disregard this constraint and allow x_a to vary in the kinematically allowed range $x_{a,\min} \leq x_a \leq 1$, where

$$x_{a,\min} = \frac{E_p E_T e^{-\eta_1}}{2E_e E_p - E_e E_T e^{\eta_1}}. \tag{6}$$

From equations (3) and (4), we can express x_b as a function of E_T, η_1, and x_a:

$$x_b = \frac{x_a E_e E_T e^{\eta_1}}{2x_a E_e E_p - E_p E_T e^{-\eta_1}}. \tag{7}$$

This function is plotted in Fig. 1 for $E_T = 20$ GeV and four different values of η_1 in the range $0 \leq \eta_1 \leq 3$ as a function of x_a. Also shown is the envelope of these curves

$$x_{b,\text{env}} = \frac{E_T^2}{x_a E_e E_p}, \tag{8}$$

which can be obtained from finding the minimum of x_b with respect to η_1 for fixed x_a. The minimal x_a-values for $\eta_1 = 0$, 1, 2, 3 are 0.379, 0.143, 0.0557, and 0.0247. The rapidity of the second jet is given by equation (5).

Depending on x_a, different regions of x_b are explored. Small values of x_b are reached for negative η_1 and the maximal possible x_a, which is $x_a = 1$ in our case and $x_a = x_{a,\max}$ in the HERA experiments. This is of interest for determining the gluon structure function of the proton in the small x region [12]. Since under experimental conditions x_a is not constrained very much, it is possible to achieve minimal values of x_b by selecting the appropriate range in E_T, η_1, and η_2 according to (3) and (4).
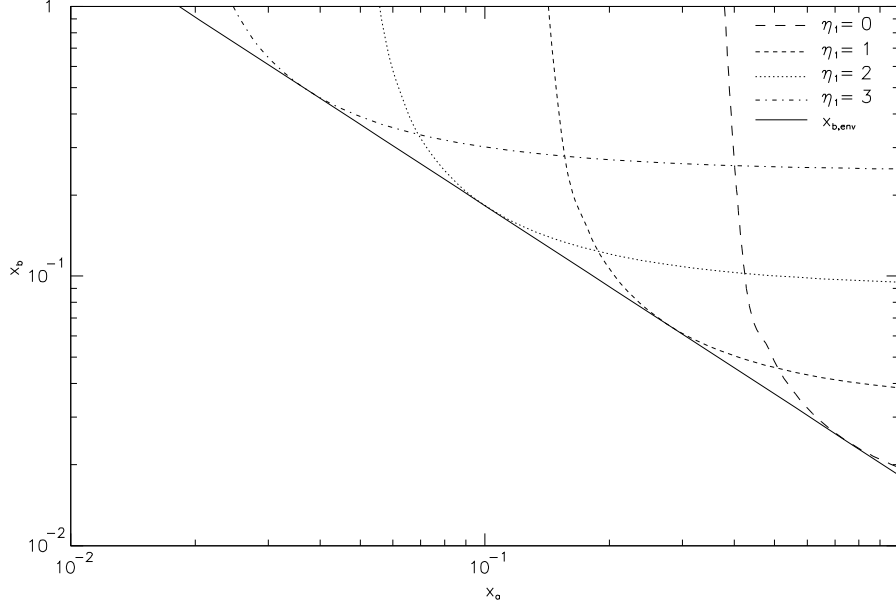
Figure 1: Contours of constant η_1 in the $x_a - x_b$ plane for $E_T = 20$ GeV. $x_{b,\mathrm{env}}$ (full curve) is the envelope of the curves.

Of course, studying the gluon structure of the proton this way depends very much on the cross sections in the appropriate regions. For direct photoproduction, the two-jet cross section for $ep \rightarrow e' + \mathrm{jet}_1 + \mathrm{jet}_2 + X$ is obtained from

$$\frac{\mathrm{d}^3\sigma}{\mathrm{d}E_T^2 \mathrm{d}\eta_1 \mathrm{d}\eta_2} = \sum_b x_a F_{\gamma/e}(x_a) x_b F_{b/p}(x_b, M_b^2) \frac{\mathrm{d}\sigma}{\mathrm{d}t}(\gamma b \rightarrow p_1 p_2). \tag{9}$$

$\mathrm{d}\sigma/\mathrm{d}t$ stands for the differential cross section of the parton subprocess $\gamma b \rightarrow p_1 p_2$. The invariants of this process are $s = (p_0 + q)^2$, $t = (p_0 - p_1)^2$, and $u = (p_0 - p_2)^2$. They can be expressed by the final state variables E_T, η_1, and η_2 and the initial state momentum fractions x_a and x_b:

$$\begin{align}
s &= 4 x_a x_b E_e E_p, \tag{10} \\
t &= -2 x_a E_e E_T e^{\eta_2} = -2 x_b E_p E_T e^{-\eta_1}, \tag{11} \\
u &= -2 x_a E_e E_T e^{\eta_1} = -2 x_b E_p E_T e^{-\eta_2}. \tag{12}
\end{align}$$

So, the dependence of the two-jet cross section on E_T, η_1, and η_2 is determined through the photon distribution function $F_{\gamma/e}$, the parton distribution functions of the proton $F_{b/p}$, and the cross sections of the hard subprocesses, which depend on s, t, and u.

For the inclusive one-jet cross section, we must integrate over one of the rapidities in (9). We integrate over η_2 and transform to the variable x_a using (3). The result is the cross section for $ep \rightarrow e' + \mathrm{jet} + X$, which depends on E_T and η:

$$\frac{\mathrm{d}^2\sigma}{\mathrm{d}E_T \mathrm{d}\eta} = \sum_b \int_{x_{a,\mathrm{min}}}^1 \mathrm{d}x_a\, x_a F_{\gamma/e}(x_a) x_b F_{b/p}(x_b, M_b^2) \frac{4 E_e E_T}{2 x_a E_e - E_T e^{-\eta}} \frac{\mathrm{d}\sigma}{\mathrm{d}t}(\gamma b \rightarrow p_1 p_2). \tag{13}$$

Here, x_b is given by (7) with $\eta_1 = \eta$.

4

The cross sections for the two subprocesses $\gamma q \to gq$ and $\gamma g \to q\bar{q}$ are well known [13] and are given by

$$\frac{\mathrm{d}\sigma}{\mathrm{d}t}(\gamma q_i \to gq_i) = \alpha\alpha_s Q_i^2 2 C_F \frac{\pi}{s^2}\left(-\frac{u}{s}-\frac{s}{u}\right), \tag{14}$$

$$\frac{\mathrm{d}\sigma}{\mathrm{d}t}(\gamma g \to q_i\bar{q}_i) = \alpha\alpha_s Q_i^2 \frac{\pi}{s^2}\left(\frac{u}{t}+\frac{t}{u}\right), \tag{15}$$

where $C_F = (N_C^2 - 1)/(2N_C)$ and N_C is the number of colors. These cross sections are $\mathrm{O}(\alpha\alpha_s)$. The index i denotes the quark flavor and Q_i the quark charge. The magnitude of the photon-gluon cross section determines whether one is sensitive to the gluon structure function of the proton.

3 Next-To-Leading Order Cross Sections

The higher order corrections are calculated as usual with the help of dimensional regularization. This method regularizes the ultraviolet singularities in the one-loop contributions, which are then subtracted using the modified minimal subtraction ($\overline{\mathrm{MS}}$) scheme. Dimensional regularization can also be used for the infrared and collinear singularities. In the following subsections, we shall consider the virtual corrections and the various real corrections needed to obtain finite cross sections in the limit dimension $n \to 4$.

3.1 Virtual Corrections up to $\mathrm{O}(\alpha\alpha_s^2)$

The one-loop diagrams for $\gamma q \to gq$ and $\gamma g \to q\bar{q}$ have an additional virtual gluon, which leads to an extra factor α_s. Interfering with the LO diagrams of order $\mathrm{O}(\alpha\alpha_s)$ produces the virtual corrections to the $2 \to 2$ cross section up to $\mathrm{O}(\alpha\alpha_s^2)$. These contributions are well known for many years from $e^+e^- \to q\bar{q}g$ higher order QCD calculations [14, 15]. For the corresponding photoproduction cross section, one substitutes $Q^2 = 0$ and performs the necessary crossings. The result can be found in [6, 16, 17]. We have also compared with the results in [11] for deep inelastic scattering $eq \to e'gq$ and $eg \to e'q\bar{q}$, which can be expressed by the invariants s, t, and u after setting $Q^2 = 0$. The structure of the corrections depends on the color factors C_F^2, $C_F N_C$, and $C_F N_f$, where N_f is the number of flavors in the $q\bar{q}$ loops. For completeness and for later use, we write the final result in the form

$$\begin{aligned}
H_V(\gamma q_i \to gq_i) = {} & e^2 g^2 \mu^{4\epsilon} 8(1-\epsilon) Q_i^2 \frac{\alpha_s}{2\pi}\left(\frac{4\pi\mu^2}{s}\right)^\epsilon \frac{\Gamma(1-\epsilon)}{\Gamma(1-2\epsilon)}\frac{1}{4} \\
& \left\{ C_F^2 V_{q1}(s,t,u) - \frac{1}{2}N_C C_F V_{q2}(s,t,u) \right. \\
& \left. + C_F\left(\frac{1}{\epsilon}+\ln\frac{s}{\mu^2}\right)\left(\frac{1}{3}N_f - \frac{11}{6}N_C\right) T_q(s,t,u)\right\} + \mathrm{O}(\epsilon),
\end{aligned} \tag{16}$$

$$\begin{aligned}
H_V(\gamma g \to q_i\bar{q}_i) = {} & e^2 g^2 \mu^{4\epsilon} 8(1-\epsilon) Q_i^2 \frac{\alpha_s}{2\pi}\left(\frac{4\pi\mu^2}{s}\right)^\epsilon \frac{\Gamma(1-\epsilon)}{\Gamma(1-2\epsilon)}\frac{1}{4} \\
& \left\{ \frac{1}{2}C_F V_{g1}(s,t,u) - \frac{1}{4}N_C V_{g2}(s,t,u) \right. \\
& \left. + \frac{1}{2}\left(\frac{1}{\epsilon}+\ln\frac{s}{\mu^2}\right)\left(\frac{1}{3}N_f - \frac{11}{6}N_C\right) T_g(s,t,u)\right\} + \mathrm{O}(\epsilon).
\end{aligned} \tag{17}$$

H_V gives the virtual corrections to the corresponding reactions up to the n-dimensional phase space factor

$$\frac{\mathrm{dPS}^{(2)}}{\mathrm{d}t} = \frac{1}{\Gamma(1-\epsilon)} \left(\frac{4\pi s}{tu}\right)^\epsilon \frac{1}{8\pi s} \tag{18}$$

and the flux factor $1/(2s)$. The expressions for V_{q1}, V_{q2}, V_{g1}, and V_{g2} are collected in appendix A. They contain singular terms $\propto 1/\epsilon^2$ and $1/\epsilon$ ($2\epsilon = 4 - n$), which are always proportional to the LO cross sections

$$T_q = (1-\epsilon)\left(-\frac{u}{s} - \frac{s}{u}\right) + 2\epsilon, \tag{19}$$

$$T_g = (1-\epsilon)\left(\frac{t}{u} + \frac{u}{t}\right) - 2\epsilon \tag{20}$$

(see eq. (14) and (15)). g is the quark-gluon coupling and μ is the renormalization scale. The terms proportional to $(\frac{1}{3}N_f - \frac{11}{6}N_C)$ result from the renormalization counter terms. The initial gluon spins are averaged by applying a factor of $1/(2(1-\epsilon))$.

3.2 Real Corrections up to $\mathrm{O}(\alpha\alpha_s^2)$

For the calculation of the hard scattering cross section up to $\mathrm{O}(\alpha\alpha_s^2)$, we must include all diagrams with an additional parton in the final state, i.e. $\gamma q \to qgg$, $\gamma q \to qq\bar{q}$, $\gamma q \to qq'\bar{q}'$, and $\gamma g \to gq\bar{q}$. The four-vectors of these subprocesses will be labeled by $qp_0 \to p_1p_2p_3$, where q is the momentum of the incoming photon and p_0 is the momentum of the incoming parton. The invariants will be denoted by $s_{ij} = (p_i + p_j)^2$ and the previously defined Mandelstam variables s, t, and u. For massless partons, the $2 \to 3$ contributions contain singularities at $s_{ij} = 0$. They can be extracted with the dimensional regularization method and cancelled against those associated with the one-loop contributions.

To achieve this we go through the following steps. First, the matrix elements for the $2 \to 3$ subprocesses are calculated in n dimensions. The corresponding diagrams are shown in Fig. 2 and are classified as I, II, ..., VII. They are squared and averaged/summed over initial/final state spins and colors and can be used for ingoing quarks, antiquarks, and gluons with the help of crossing. The diagrams III' account for ghosts to cancel unphysical polarizations of the gluons. This classification is the same as in ref. [11]. Since the hadronic tensor is symmetric, we need to consider only the products I·I, II·I, III·I etc. Furthermore, the products V·IV, VI·IV, VII·IV, VI·V, VII·V, and VII·VI are not singular and vanish with the cut-off describing the boundary of the singular region. Such terms will be neglected consistently in the following.

Next, one can distinguish three classes of singularities in photoproduction ($Q^2 \simeq 0$) depending on which propagators in the squared matrix elements vanish. Examples for these three classes are shown in Fig. 3. The X marks the propagator leading to the divergence. In the first graph, it is the invariant s_{23} given by momenta of the final state. Therefore, this singularity will be called final state singularity. The second graph becomes singular for $s_{q1} = (q+p_1)^2 = 0$, when the photon and the final quark momentum are parallel. This is the class of photon initial state singularities. In the third graph, the singularity occurs at $s_{03} = (p_0 + p_3)^2$, where p_0 is the initial parton momentum. This stands for parton initial state singularity. The first class is familiar from similar calculations for jet production in e^+e^- annihilation [16], the third class from jet production in deep inelastic ep scattering ($Q^2 \neq 0$) [11]. The second class occurs only
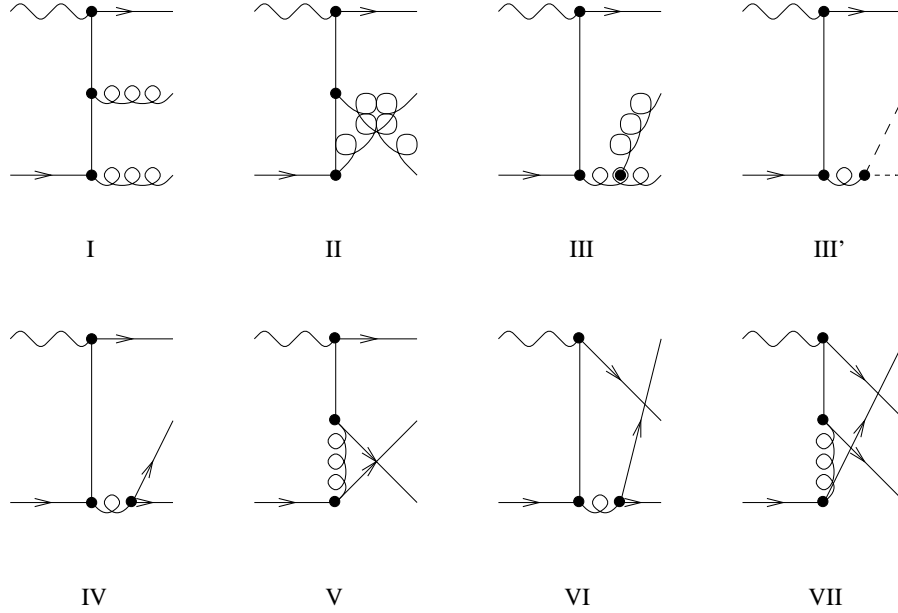
6

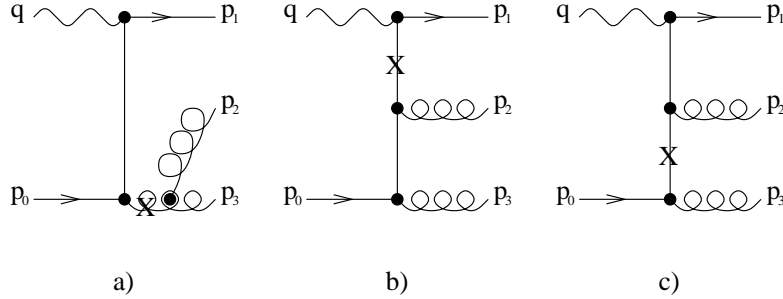Figure 2: Three-body diagrams for classes I, ..., VII as described in the text.

Figure 3: Three-body diagrams with final and initial state singularities.

for photoproduction [9, 10].

When squaring the sum of all diagrams in Fig. 2, we encounter terms, where more than one of the invariants become singular, e.g. when one of the gluon momenta $p_3 \to 0$ so that $s_{23} = 0$ and $s_{03} = 0$. These infrared singularities are disentangled by a partial fractioning decomposition, so that every term has only one vanishing denominator. This also allows the separation of the different classes of singularities in Fig. 3. Except for additional terms separating the photon initial state singularity, we follow the procedure in [11]. It turns out that the results are always proportional to the LO cross sections involved in the hard scatter like T_q and T_g in eq. (19) and (20)

$$H_{F,I,J} = KT_i. \tag{21}$$

Here, F, I, and J denote final state, photon initial state and proton initial state contributions.

As the last step, the decomposed matrix elements have to be integrated up to $s_{ij} \le ys$. y

7

characterizes the region, where the two partons i and j cannot be resolved. Then, the singular kernel K produces terms $\propto 1/\epsilon^2$ and $1/\epsilon$, which will cancel against those in the virtual diagrams or be absorbed into structure functions, and finite corrections proportional to $\ln^2 y$, $\ln y$, and y^0. Terms of $O(y)$ will be neglected. In the following, we shall give the results for the different classes of singularities separately.

3.2.1 Final State Singularities

In this section, we assume that after partial fractioning the $2 \to 3$ matrix elements are singular only for $s_{12} = 0$. For the integration over the singular region of phase space, we choose as the coordinate system the c.m. system of partons p_1 and p_2. The angles of the other parton three-momenta p_0 and p_3 with respect to p_1 and p_2 are shown in Fig. 4. χ is the angle between p_0 and p_3, θ is the angle between p_0 and p_1, and ϕ is the azimuthal angle between the planes defined by p_0 and p_1 and p_0 and p_3, respectively.
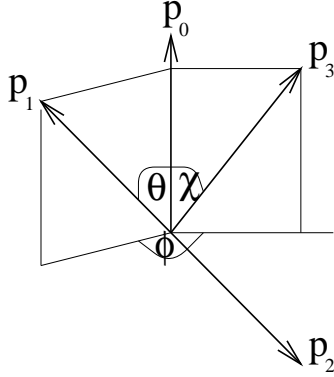

Figure 4: Diagram for the three-body final state defining the kinematical variables in the c.m. system of partons p_1 and p_2.

In general, the invariants

$$s = (p_0 + q)^2, \tag{22}$$
$$t = (p_0 - p_1 - p_2)^2 - 2p_1p_2, \tag{23}$$
$$u = (p_0 - p_3)^2 \tag{24}$$

differ from the corresponding two-body invariants (see eq. (10)-(12)), but approach them for $p_2 = 0$ or p_2 parallel to p_1. Then, $t = (p_0 - \bar{p}_1)^2$ and $u = (p_0 - p_3)^2$, where $\bar{p}_1 = p_1 + p_2$ is the four-momentum of the recombined jet and p_3 is the four-momentum of the second jet. This produces a jet mass $\bar{p}_1^2 = (p_1 + p_2)^2 \neq 0$, which vanishes in the limit $y \to 0$. For $p_2 = 0$, we have $\bar{p}_1 = p_1$, and for p_2 parallel to p_1 we have $\bar{p}_1 \propto p_1$. The definitions of t and u are unique only in the limit $s_{12} \to 0$. Other choices for the three-parton final state variables differ by finite contributions of $O(y)$, which are neglected throughout. We substitute the angle θ by

$$b = \frac{1}{2}(1 - \cos\theta) \tag{25}$$

8

and introduce the new variable

$$z' = \frac{p_1 p_2}{p_0 q}.$$ (26)

The three-body phase space in n dimensions can be factorized into two two-body phase space terms [11]

$$\mathrm{dPS}^{(3)} = \mathrm{dPS}^{(2)} \mathrm{dPS}^{(r)},$$ (27)

where

$$\frac{\mathrm{dPS}^{(2)}}{\mathrm{d}t} = \frac{1}{\Gamma(1-\epsilon)} \left(\frac{4\pi s}{tu}\right)^\epsilon \frac{1}{8\pi s}$$ (28)

and

$$\mathrm{dPS}^{(r)} = \left(\frac{4\pi}{s}\right)^\epsilon \frac{\Gamma(1-\epsilon)}{\Gamma(1-2\epsilon)} \frac{s}{16\pi^2} \frac{1}{1-2\epsilon} \mathrm{d}\mu_F$$ (29)

with

$$\mathrm{d}\mu_F = \mathrm{d}z' z'^{-\epsilon} \left(1 + \frac{z's}{t}\right)^{-\epsilon} \frac{\mathrm{d}b}{N_b} b^{-\epsilon}(1-b)^{-\epsilon} \frac{\mathrm{d}\phi}{N_\phi} \sin^{-2\epsilon}\phi.$$ (30)

N_b and N_ϕ are normalization factors:

$$N_b = \int_0^1 \mathrm{d}b (b(1-b))^{-\epsilon} = \frac{\Gamma^2(1-\epsilon)}{\Gamma(2-2\epsilon)},$$ (31)

$$N_\phi = \int_0^\pi \sin^{-2\epsilon}\phi \mathrm{d}\phi = \frac{\pi 4^\epsilon \Gamma(1-2\epsilon)}{\Gamma^2(1-\epsilon)}.$$ (32)

$\mathrm{dPS}^{(2)}$ is the same phase space factor as in the two-body LO final state. The full range of integration in $\mathrm{dPS}^{(r)}$ is given by $z' \in [0, -t/s]$, $b \in [0, 1]$, and $\phi \in [0, \pi]$. The singular region is defined by the requirement that partons p_1 and p_2 are recombined, i.e. $p_2 = 0$ or p_2 parallel to p_1, so that $s_{12} = 0$. We integrate over this region up to $s_{12} \leq ys$, which restricts the range of z' to $0 \leq z' \leq \min\{-t/s, y\} \equiv y_F$.

The matrix elements, which are obtained by squaring the sum of diagrams in Fig. 2, are expressed by the variables s, t, u, z', b, and ϕ. Depending on the structure of the interfering diagrams and the color factors, we distinguish seven types of contributions: F_1, F_2, ..., F_7. Five of them are for an incoming quark or antiquark and two for an incoming gluon. The definition of the F_i with the corresponding color factors can be read off Tab. 1.

In class F_1, we have QED-type diagrams proportional to C_F^2, where a gluon can become soft or collinear with a quark. F_2 contains QED-type diagrams and interference terms with diagrams containing a three-gluon vertex proportional to $C_F N_C$. Class F_3 stands for contributions of this latter type, where the infrared divergence is caused by the two-gluon final state. F_4 has only contributions from non-abelian diagrams, and F_5 contains the four-quark diagrams. In this class, the divergence originates from the collinear $q\bar{q}$ pair. In F_6 and F_7, we have contributions with incoming gluons proportional to C_F and N_C, respectively. We emphasize that this classification rests upon the use of the Feynman gauge for the gluon spin summation with all ghost contributions included. Of course, the sum of all terms is gauge invariant.

After integrating the $2 \to 3$ matrix elements with final state singularities H_{F_i}, we obtain

$$\int \mathrm{dPS}^{(r)} H_{F_i} = e^2 g^2 \mu^{4\epsilon} 8(1-\epsilon) Q_i^2 \frac{\alpha_s}{2\pi} \left(\frac{4\pi\mu^2}{s}\right)^\epsilon \frac{\Gamma(1-\epsilon)}{\Gamma(1-2\epsilon)} \frac{1}{4} F_i + \mathrm{O}(\epsilon).$$ (33)

Class	Inc. Parton	Diagrams	Color Factor
F_1	Quark	I·I, II·II, II·I	$N_C C_F^2/N_C$
F_2	Quark	II·I, III·I, III·II	$-1/2\ N_C^2 C_F/N_C$
F_3	Quark	III·I, III·II	$-1/2\ N_C^2 C_F/N_C$
F_4	Quark	III·III	$N_C^2 C_F/N_C$
F_5	Quark	IV·IV, V·V, VI·VI, VII·VII	$1/2\ N_C C_F/N_C$
F_6	Gluon	I·I, II·II, II·I	$N_C C_F^2/2N_C C_F$
F_7	Gluon	II·I, III·I, III·II	$-1/2\ N_C^2 C_F/2N_C C_F$

Table 1: Classification of the $2 \to 3$ matrix elements for final state singularities

The final results for the F_i are written down in appendix B. They contain the infrared and collinear singularities which cancel against those in the virtual corrections. At this point, it is essential that the singular terms are all proportional to the LO matrix elements $T_q(s,t,u)$ and $T_g(s,t,u)$ and that the variables s, t, and u defined in (22)-(24) correspond to the two-body variables in the infrared and collinear limit with an appropriate definition of the recombined jet momentum.

3.2.2 Photon Initial State Singularities

To integrate over the singularity $s_{q3} = 0$, we use the same p_1, p_2 c.m. coordinate system as in the last section. Let us assume that we have isolated the terms in the three-body cross sections with a singularity at $s_{q3} = 0$, i.e. where the outgoing quark momentum p_3 is collinear with the photon momentum q. In this case, the quark p_3 is part of the photon remnant and p_1 and p_2 are the parton momenta of the two-body subprocess. We introduce a new variable

$$z_a = \frac{p_1 p_2}{p_0 q} \in [X_a, 1], \tag{34}$$

where $X_a = \frac{p_1 p_2}{p_0 p_e} \simeq E_q/E_e$ is now the fraction of the initial electron energy transferred to the quark in the hard scatter. Then, z_a parametrizes the phase space of the collinear quark $p_3 = (1 - z_a)q$ and renders the Mandelstam variables in the form

$$s = (p_0 + z_a q)^2, \tag{35}$$
$$t = (p_0 - p_1)^2, \tag{36}$$
$$u = (p_0 - p_2)^2. \tag{37}$$

With the additional variable

$$z'' = \frac{q p_3}{q p_0}, \tag{38}$$

the three-body phase space factorizes into

$$\mathrm{dPS}^{(3)} = \mathrm{dPS}^{(2)}\mathrm{dPS}^{(r)}. \tag{39}$$

$\mathrm{dPS}^{(2)}$ is identical to (28), and

$$\mathrm{dPS}^{(r)} = \left(\frac{4\pi}{s}\right)^\epsilon \frac{\Gamma(1 - \epsilon)}{\Gamma(1 - 2\epsilon)} \frac{s}{16\pi^2} H_a(z'')\mathrm{d}\mu_I, \tag{40}$$

10

where

$$d\mu_I = dz'' z''^{-\epsilon} \frac{dz_a}{z_a} \left(\frac{z_a}{1 - z_a} \right)^{\epsilon} \frac{d\phi}{N_\phi} \sin^{-2\epsilon} \phi \frac{\Gamma(1 - 2\epsilon)}{\Gamma^2(1 - \epsilon)} \quad (41)$$

and

$$H_a(z'') = \left(1 + \frac{z''}{z_a} \right)^{-1+2\epsilon} \left(1 - \frac{z''}{1 - z_a} \right)^{-\epsilon} = 1 + \mathrm{O}(z'') \quad (42)$$

can be approximated by 1 as it leads only to negligible terms of $\mathrm{O}(y)$. The full region of integration is given by $z'' \in [0, -u/s]$, $z_a \in [X_a, 1]$, and $\phi \in [0, \pi]$, whereas the singular region is defined by the requirement that parton p_3 is collinear to q, so that $s_{q3} < ys/z_a$. This restricts the range of z'' to $0 \leq z'' \leq \min\{-u/s, y\} \equiv y_I$.

The matrix elements from Fig. 2 can be put into seven classes $I_1, I_2, ..., I_7$ displayed in Tab. 2. The classification is again according to incoming parton, color factor, and general structure.

Class	Inc. Parton	Diagrams	Color Factor
I_1	Quark	I·I, II·II, II·I	$N_C C_F^2 / N_C$
I_2	Quark	II·I, III·I, III·II	$-1/2\, N_C^2 C_F / N_C$
I_3	Quark	IV·IV, V·V, VI·VI, VII·VII	$1/2\, N_C C_F / N_C$
I_4	Quark	IV·IV, V·V, VI·VI, VII·VII	$1/2\, N_C C_F / N_C$
I_5	Quark	IV·IV, V·V, VI·VI, VII·VII	C_F / N_C
I_6	Gluon	I·I, II·II, II·I	$N_C C_F^2 / 2 N_C C_F$
I_7	Gluon	II·I, III·I, III·II	$-1/2\, N_C^2 C_F / 2 N_C C_F$

Table 2: Classification of the $2 \to 3$ matrix elements for photon initial state singularities

In all classes, the incoming photon can become collinear to a quark line only, since there is no direct coupling to a gluon line. Furthermore, there are only single poles, i.e. only collinear singularities. The three-body matrix elements are factorized into LO two-body parton-parton scattering matrix elements and a singular kernel K. Since the quark (antiquark) produced by the photon becomes part of the photon remnant, the remaining two-body process is induced by an antiquark (quark) in the initial state, which interacts with a quark or antiquark of the same or different flavor or a gluon from the proton. The factorized LO parton-parton scattering cross sections are given by the functions $U_i(s, t, u)$ $(i = 1, 2, 3)$ related to the various processes as in Tab. 3.

The functions $U_i(s, t, u)$ are decomposed with respect to their color structure as follows:

$$
\begin{aligned}
U_1 &= \left(C_F - N_C \frac{ut}{s^2} \right)(1 - \epsilon) \left[(1 - \epsilon)\left(\frac{t}{u} + \frac{u}{t} \right) - 2\epsilon \right] \quad (43) \\
&= C_F T_{1a}(s, t, u) - \frac{N_C}{2} T_{1b}(s, t, u), \\
U_2 &= \frac{1}{2}\left(\frac{s^2 + u^2}{t^2} - \epsilon \right) = \frac{1}{2} T_2(s, t, u), \quad (44) \\
U_3 &= -\frac{1}{N_C}(1 - \epsilon)\left(\frac{s^2}{tu} + \epsilon \right) = \frac{1}{N_C} T_3(s, t, u). \quad (45)
\end{aligned}
$$

11

Process	Matrix element $|\mathcal{M}|^2 = 8N_C C_F g^4 U_i$
$q\bar{q} \to gg$	$U_1(s,t,u)$
$qq' \to qq'$	$U_2(s,t,u)$
$q\bar{q}' \to q\bar{q}'$	$U_2(u,t,s)$
$q\bar{q} \to q'\bar{q}'$	$U_2(t,s,u)$
$qq \to qq$	$U_2(s,t,u) + U_2(s,u,t) + U_3(s,t,u)$
$q\bar{q} \to q\bar{q}$	$U_2(u,t,s) + U_2(u,s,t) + U_3(u,t,s)$
$qg \to qg$	$-U_1(t,s,u)$

Table 3: LO parton-parton scattering matrix elements

The functions T_{1a}, T_{1b}, T_2, and T_3 appear in the final result

$$\int \mathrm{dPS}^{(r)} H_{I_i} = \int_{X_a}^1 \frac{\mathrm{d}z_a}{z_a} e^2 g^2 \mu^{4\epsilon} 8(1-\epsilon) \frac{\alpha_s}{2\pi} \left(\frac{4\pi\mu^2}{s}\right)^\epsilon \frac{\Gamma(1-\epsilon)}{\Gamma(1-2\epsilon)} \frac{1}{4} I_i + \mathrm{O}(\epsilon), \qquad (46)$$

which is obtained from the integration of the decomposed matrix elements H_{I_i} over $\mathrm{dPS}^{(r)}$. It is clear that the photon initial state singularities lead to contributions familiar from LO resolved photoproduction.

The terms I_i are collected in appendix C and show explicitly the poles in $1/\epsilon$ proportional to

$$P_{q_i \leftarrow \gamma}(z_a) = 2N_C Q_i^2 \frac{1}{2} \left[z_a^2 + (1-z_a)^2\right]. \qquad (47)$$

This function appears in the evolution equation of the photon structure function as an inhomogeneous or so-called point-like term. Therefore, the photon initial state singularities can be absorbed into the photon structure function. The necessary steps are well known [16, 18]. We define the renormalized distribution function of a parton a in the electron $F_{a/e}(X_a, M_a^2)$ as

$$F_{a/e}(X_a, M_a^2) = \int_{X_a}^1 \frac{\mathrm{d}z_a}{z_a} \left[\delta_{a\gamma}\delta(1-z_a) + \frac{\alpha}{2\pi} R_{a\leftarrow\gamma}(z_a, M_a^2)\right] F_{\gamma/e}\left(\frac{X_a}{z_a}\right), \qquad (48)$$

where R has the general form

$$R_{a\leftarrow\gamma}(z_a, M_a^2) = -\frac{1}{\epsilon} P_{a\leftarrow\gamma}(z_a) \frac{\Gamma(1-\epsilon)}{\Gamma(1-2\epsilon)} \left(\frac{4\pi\mu^2}{M_a^2}\right)^\epsilon + C_{a\leftarrow\gamma}(z_a) \qquad (49)$$

with $C = 0$ in the $\overline{\mathrm{MS}}$ scheme. The renormalized partonic cross section for $\gamma b \to$ jets is then calculated from

$$\mathrm{d}\sigma(\gamma b \to \mathrm{jets}) = \mathrm{d}\bar{\sigma}(\gamma b \to \mathrm{jets}) - \frac{\alpha}{2\pi} \int \mathrm{d}z_a R_{a\leftarrow\gamma}(z_a, M_a^2) \mathrm{d}\sigma(ab \to \mathrm{jets}). \qquad (50)$$

$\mathrm{d}\bar{\sigma}(\gamma b \to \mathrm{jets})$ is the higher order cross section before the subtraction procedure, and $\mathrm{d}\sigma(ab \to \mathrm{jets})$ contains the LO parton-parton scattering matrix elements $U_i(s,t,u)$. The factor $\frac{4\pi\mu^2}{M_a^2}$ in (49) is combined with the factor $\frac{4\pi\mu^2}{s}$ in (46) and leads to M_a^2 dependent terms of the form

$$-\frac{1}{\epsilon} P_{a\leftarrow\gamma}(z_a) \left[\left(\frac{4\pi\mu^2}{s}\right)^\epsilon - \left(\frac{4\pi\mu^2}{M_a^2}\right)^\epsilon\right] = -P_{a\leftarrow\gamma}(z_a) \ln\left(\frac{M_a^2}{s}\right), \qquad (51)$$

so that the cross section after subtraction in (50) will depend on the factorization scale M_a^2.

3.2.3 Parton Initial State Singularities

The computation of the parton initial state contributions is very similar to the last section. We again use the p_1, p_2 c.m. coordinate system as defined in Fig. 4. Singularities occur in this case for $s_{03} = 0$, when the incoming parton p_0 radiates a soft gluon ($p_3 = 0$) or a collinear parton p_3. The new variable

$$z_b = \frac{p_1 p_2}{p_0 q} \in [X_b, 1] \tag{52}$$

describes the momentum of parton $p_3 = (1 - z_b)p_0$ and the reduced momentum of the parton involved in the hard scatter $z_b p_0$. $X_b = \frac{p_1 p_2}{Pq} \simeq E_{q/g}/E_p$ is the energy fraction of the incoming proton involved in the $2 \to 2$ subprocess. The corresponding invariants are

$$s = (z_b p_0 + q)^2, \tag{53}$$
$$t = (z_b p_0 - p_1)^2, \tag{54}$$
$$u = (z_b p_0 - p_2)^2. \tag{55}$$

Using the variable

$$z''' = \frac{p_0 p_3}{p_0 q}, \tag{56}$$

we can again factorize the three-body phase space into

$$\mathrm{dPS}^{(3)} = \mathrm{dPS}^{(2)} \mathrm{dPS}^{(r)}, \tag{57}$$

where $\mathrm{dPS}^{(2)}$ stands for (28).

$$\mathrm{dPS}^{(r)} = \left(\frac{4\pi}{s}\right)^{\epsilon} \frac{\Gamma(1 - \epsilon)}{\Gamma(1 - 2\epsilon)} \frac{s}{16\pi^2} H_b(z''') \mathrm{d}\mu_J, \tag{58}$$

where

$$\mathrm{d}\mu_J = \mathrm{d}z''' z'''^{-\epsilon} \frac{\mathrm{d}z_b}{z_b} \left(\frac{z_b}{1 - z_b}\right)^{\epsilon} \frac{\mathrm{d}\phi}{N_\phi} \sin^{-2\epsilon} \phi \frac{\Gamma(1 - 2\epsilon)}{\Gamma^2(1 - \epsilon)} \tag{59}$$

and

$$H_b(z''') = (1 - z''')^{-1+2\epsilon} \left(1 - \frac{z'''}{1 - z_b}\right)^{-\epsilon} = 1 + \mathrm{O}(z''') \tag{60}$$

can again be approximated by 1. The integration over $z''' \in [0, -u/s]$, $z_b \in [X_b, 1]$, and $\phi \in [0, \pi]$ is restricted to the singular region of z''' in the range $0 \leq z''' \leq \min\{-u/s, y\} \equiv y_J$.

The three-body matrix elements can be computed from Fig. 2 and classified according to color factor, incoming parton, and type of parton participating in the two-body process as in Tab. 4. In the case of final state singularities considered in section 3.2.1, the ingoing parton (quark or gluon) was always the ingoing parton of the two-body subprocess. As could already been seen in the last section, this is not the case for initial state singularities. For example, if an ingoing quark is collinear to the outgoing gluon (quark), the factorized 2-jet matrix element has an initial quark (gluon).

In Tab. 4, J_1 is the class of QED type terms, where a gluon in the final state is collinear with the initial state quark. The same occurs in J_2, where QED-type and non-abelian diagrams interfere. J_3 contains the four-quark diagrams, in which an outgoing quark is collinear with

13

Class	Inc. Parton (3-jet)	Inc. Parton (2-jet)	Diagrams	Color Factor
J_1	Quark	Quark	I·I, II·II, II·I	$N_C C_F^2/N_C$
J_2	Quark	Quark	II·I, III·I, III·II	$-1/2\, N_C^2 C_F/N_C$
J_3	Quark	Gluon	IV·IV, V·V, VI·VI, VII·VII	$1/2\, N_C C_F/N_C$
J_4	Gluon	Quark	I·I, II·II, II·I	$N_C C_F^2/2N_C C_F$
J_5	Gluon	Quark	II·I, III·I, III·II	$-1/2\, N_C^2 C_F/2N_C C_F$
J_6	Gluon	Gluon	II·I, III·I, III·II	$-1/2\, N_C^2 C_F/2N_C C_F$
J_7	Gluon	Gluon	III·III	$N_C^2 C_F/2N_C C_F$

Table 4: Classification of the $2 \to 3$ matrix elements for parton initial state singularities

an ingoing quark. In J_4 and J_5, we have an ingoing gluon and an outgoing collinear quark. The classes differ only by their color factors. In J_6 and J_7, an outgoing gluon is collinear with the ingoing gluon, where J_6 contains QED-type and interference terms and J_7 contains pure non-abelian terms.

The next step is to perform the z''' integration with the upper limit y_J. The result can be written in the form

$$\int \mathrm{dPS}^{(r)} H_{J_i} = \int_{X_b}^1 \frac{\mathrm{d}z_b}{z_b} e^2 g^2 \mu^{4\epsilon} 8(1-\epsilon) Q_i^2 \frac{\alpha_s}{2\pi} \left(\frac{4\pi\mu^2}{s}\right)^\epsilon \frac{\Gamma(1-\epsilon)}{\Gamma(1-2\epsilon)} \frac{1}{4} J_i + \mathrm{O}(\epsilon), \qquad (61)$$

where the J_i are given in appendix D. Besides s, t, u, and y_J, they still depend on the integration variable z_b. The singular parts take the form

$$J_1 = \left[-\frac{1}{\epsilon}\frac{1}{C_F}P_{q\leftarrow q}(z_b) + \delta(1-z_b)\left(\frac{1}{\epsilon^2} + \frac{1}{\epsilon}\left(-\ln\frac{-t}{s} + \frac{3}{2}\right)\right)\right] C_F^2 T_q(s,t,u) + \mathrm{O}(\epsilon^0), \quad (62)$$

$$J_2 = \left[\delta(1-z_b)\frac{1}{\epsilon}\ln\frac{u}{t}\right]\left(-\frac{1}{2}N_C C_F\right) T_q(s,t,u) + \mathrm{O}(\epsilon^0), \tag{63}$$

$$J_3 = \left[-\frac{1}{\epsilon}\frac{1}{C_F}P_{g\leftarrow q}(z_b)\right]\frac{C_F}{2}T_g(s,t,u) + \mathrm{O}(\epsilon^0), \tag{64}$$

$$J_4 = \left[-\frac{2}{\epsilon}P_{q\leftarrow g}(z_b)\right] C_F T_q(s,t,u) + \mathrm{O}(\epsilon^0), \tag{65}$$

$$J_6 = \left[\frac{2}{\epsilon}\frac{1}{N_C}P_{g\leftarrow g}(z_b) + \delta(1-z_b)\left(-\frac{2}{\epsilon^2} + \frac{1}{\epsilon}\left(\ln\frac{tu}{s^2} - \frac{2}{N_C}\left(\frac{11}{6}N_C - \frac{1}{3}N_f\right)\right)\right)\right] \tag{66}$$
$$\left(-\frac{N_C}{4}\right) T_g(s,t,u) + \mathrm{O}(\epsilon^0).$$

J_5 is $\mathrm{O}(\epsilon)$ and does not contribute. J_6 contains contributions from J_6 as well as J_7. Some of the J_i contain infrared singularities $\propto 1/\epsilon^2$, which must cancel against the corresponding singularities in the virtual contributions. The singular parts are decomposed in such a way that the Altarelli-Parisi kernels in four dimensions proportional to $1/\epsilon$ are split off. They also appear in the evolution equations for the parton distribution functions and are defined explicitly in appendix D. The singular terms proportional to these kernels are absorbed as usual into the scale dependent structure functions

$$F_{b/p}(X_b, M_b^2) = \int_{X_b}^1 \frac{\mathrm{d}z_b}{z_b}\left[\delta_{bb'}\delta(1-z_b) + \frac{\alpha_s}{2\pi}R'_{b\leftarrow b'}(z_b, M_b^2)\right] F_{b'/p}\left(\frac{X_b}{z_b}\right), \tag{67}$$

14

where $F_{b'/p}\left(\frac{X_b}{z_b}\right)$ is the LO structure function before absorption of the collinear singularities and

$$R'_{b\leftarrow b'}(z_b, M_b^2) = -\frac{1}{\epsilon}P_{b\leftarrow b'}(z_b)\frac{\Gamma(1-\epsilon)}{\Gamma(1-2\epsilon)}\left(\frac{4\pi\mu^2}{M_b^2}\right)^{\epsilon} + C'_{b\leftarrow b'}(z_b) \tag{68}$$

with $C' = 0$ in the $\overline{\text{MS}}$ scheme. Then, the renormalized higher order hard scattering cross section $d\sigma(\gamma b \to \text{jets})$ is calculated from

$$d\sigma(\gamma b \to \text{jets}) = d\bar{\sigma}(\gamma b \to \text{jets}) - \frac{\alpha_s}{2\pi}\int dz_b R'_{b\leftarrow b'}(z_b, M_b^2)d\sigma(\gamma b' \to \text{jets}). \tag{69}$$

$d\bar{\sigma}(\gamma b \to \text{jets})$ is the higher order cross section before the subtraction procedure, and $d\sigma(\gamma b' \to \text{jets})$ contains the lowest order matrix elements $T_q(s,t,u)$ and $T_g(s,t,u)$ in n dimensions. This well known factorization prescription [18] removes finally all remaining collinear singularities. It is universal and leads for all processes to the same definition of structure functions if the choice concerning the regular function C' in (68) is kept fixed. Similar to the case of photon initial state singularities, the higher order cross sections in (69) will depend on the factorization scale M_b due to terms of the form $P_{b\leftarrow b'}(z_b)\ln\left(\frac{M_b^2}{s}\right)$.

3.3 Jet Cross Sections in NLO

To obtain a finite cross section, we must add the four parts considered in sections 3.1 and 3.2.1-3.2.3. Then, the poles in $1/\epsilon$ must cancel, and we can take the limit $\epsilon \to 0$. The result is a special kind of two-jet cross section, where the recombination of two partons into one jet or the recombination of a parton with the photon or proton remnant jet is done with an invariant mass cut-off y. In LO, this cross section was written down in (9). Including the NLO corrections, it has the form

$$\begin{aligned}\frac{d^3\sigma}{dE_T^2 d\eta_1 d\eta_2} &= \sum_b x_a F_{\gamma/e}(x_a)\left[x_b F_{q/p}(x_b, M_b^2)\frac{d\sigma}{dt}(\gamma q \to p_1 p_2) + \frac{d\tilde{\sigma}}{dt}(\gamma q \to p_1 p_2)\right.\\ &\quad + x_b F_{g/p}(x_b, M_b^2)\frac{d\sigma}{dt}(\gamma g \to p_1 p_2) + \frac{d\tilde{\sigma}}{dt}(\gamma g \to p_1 p_2)\\ &\quad \left. + x_b F_{b/p}(x_b, M_b^2)\frac{d\tilde{\sigma}}{dt}(ab \to p_1 p_2)\right].\end{aligned} \tag{70}$$

In (70), $\frac{d\sigma}{dt}(\gamma q \to p_1 p_2)$ and $\frac{d\sigma}{dt}(\gamma g \to p_1 p_2)$ stand for two-body contributions in LO and NLO together with analytically integrated contributions of the soft and collinear divergent regions of the three-parton final state. The contributions from the photon initial state singularities are denoted $\frac{d\tilde{\sigma}}{dt}(ab \to p_1 p_2)$. $\frac{d\tilde{\sigma}}{dt}(\gamma q \to p_1 p_2)$ and $\frac{d\tilde{\sigma}}{dt}(\gamma g \to p_1 p_2)$ originate from the integration of the soft and collinear singularities of the parton initial state.

The quark induced cross section can be written as

$$\frac{d\sigma}{dt}(\gamma q \to p_1 p_2) = \alpha_s(\mu^2)CT_q + \frac{\alpha_s^2(\mu^2)}{2\pi}C(T_q A_q + B_q), \tag{71}$$

where

$$A_q = -\frac{1}{6}(11N_C - 2N_f)\ln\frac{s}{\mu^2} + \frac{N_f}{3}\left(\ln y_F - \frac{5}{3}\right) - N_C\frac{11}{6}\ln y_F \tag{72}$$

15

$$+ (2C_F - N_C) \left[\frac{1}{2} \ln^2 \frac{t}{u} - \frac{1}{4} \ln^2 \frac{-t}{s} + \ln y_F \ln \frac{-t}{s} - \text{Li}_2 \left(\frac{y_F s}{t} \right) \right]$$

$$+ N_C \left[-\frac{1}{2} \ln^2 y_F - \frac{1}{2} \ln^2 \frac{y_F s}{-u} + \frac{1}{4} \ln^2 \frac{-u}{s} - \text{Li}_2 \left(\frac{y_F s}{u} \right) + \frac{67}{18} - \frac{\pi^2}{2} \right]$$

$$+ C_F \left[\frac{\pi^2}{3} - \frac{7}{2} - \ln^2 y_F - \frac{3}{2} \ln y_F \right] ,$$

$$B_q = -3 C_F \frac{s}{u} \ln \frac{-u}{s} - \frac{1}{2} (2C_F - N_C) \left[2 \ln \frac{-us}{t^2} + \left(2 + \frac{u}{s} \right) \left(\pi^2 + \ln^2 \frac{t}{u} \right) \right. \tag{73}$$

$$\left. + \left(2 + \frac{s}{u} \right) \ln^2 \frac{-t}{s} \right] ,$$

$$T_q = -\frac{u}{s} - \frac{s}{u}, \text{ and } C = \frac{2\pi\alpha}{s^2} Q_i^2 C_F. \tag{74}$$

For the gluon induced cross section, we have

$$\frac{d\sigma}{dt}(\gamma g \to p_1 p_2) = \frac{3}{8} \alpha_s(\mu^2) C T_g + \frac{3}{8} \frac{\alpha_s^2(\mu^2)}{2\pi} C (T_g A_g + B_g), \tag{75}$$

where

$$A_g = -\frac{1}{6} (11 N_C - 2 N_f) \ln \frac{s}{\mu^2} + C_F \left[\ln^2 \frac{-t}{s} + \ln^2 \frac{-u}{s} - 2 \ln^2 y_F - 3 \ln y_F \right] \tag{76}$$

$$+ N_C \left[-\frac{1}{2} \ln^2 \frac{tu}{s^2} - \frac{\pi^2}{6} - \frac{1}{2} \ln^2 \frac{y_F s}{-t} - \frac{1}{2} \ln^2 \frac{y_F s}{-u} + \ln^2 y_F + \frac{1}{4} \ln^2 \frac{-t}{s} + \frac{1}{4} \ln^2 \frac{-u}{s} \right.$$

$$\left. - \text{Li}_2 \left(\frac{y_F s}{t} \right) - \text{Li}_2 \left(\frac{y_F s}{u} \right) \right] ,$$

$$B_g = 3 C_F \left(\frac{t}{u} \ln \frac{-u}{s} + \frac{u}{t} \ln \frac{-t}{s} \right) + \frac{1}{2} (2C_F - N_C) \left[2 \ln \frac{tu}{s^2} + \left(2 + \frac{u}{t} \right) \ln^2 \frac{-u}{s} \right. \tag{77}$$

$$\left. + \left(2 + \frac{t}{u} \right) \ln^2 \frac{-t}{s} \right] ,$$

$$T_g = \frac{t}{u} + \frac{u}{t}. \tag{78}$$

The cut dependence of the final state NLO corrections in A_q and A_g is contained in the y_F dependent terms. For $y_F \to 0$, these terms behave like $(-\ln^2 y_F)$, which leads to unphysical negative cross sections for very small y_F. Thus if y is used as a physical cut, it must be sufficiently large. In most of the applications, we shall use these results for computing inclusive cross sections, in which the y dependence of the two-jet cross section cancels against the y dependence of the numerically calculated three-jet cross section. The quadratic terms in $(\ln y_F)$ are connected with the soft divergence of the three-parton final state.

The contributions from the photon initial state singularities necessarily have a photon remnant. They depend on the cut-off y_I only through terms proportional to $(\ln y_I)$. This contribution can be considered separately only if y_I is a physical cut, i.e. if it is sufficiently large. In case one introduces other kinematical conditions to define the photon remnant terms in the NLO direct cross section, one must add the appropriate three-body contributions. The two-jet cross section is calculated from

$$\frac{d\tilde{\sigma}}{dt}(ab \to p_1 p_2) = \frac{d\hat{\sigma}}{dt}(ab \to p_1 p_2) \frac{\alpha}{2\pi} \tag{79}$$

$$\int_{X_a}^1 \frac{dz_a}{z_a} \left[P_{q_i \leftarrow \gamma}(z_a) \left(\ln \left(\frac{(1 - z_a) y_I s}{z_a M_a^2} \right) - 1 \right) + 2 N_C \frac{Q_i^2}{2} \right] .$$

16

In (79), M_a is the factorization scale at the photon leg. This dependence must cancel against the M_a dependence of the LO resolved contribution (see eq. (48)). This has been demonstrated explicitly in [19] for the inclusive single jet cross section. The $\frac{\mathrm{d}\hat{\sigma}}{\mathrm{d}t}(ab \rightarrow p_1 p_2)$ are the cross sections for the $2 \rightarrow 2$ subprocesses which were given in section 3.2.2 in terms of the functions $U_i(s,t,u)$. These are the well known LO cross sections also used for the calculation of hadron-hadron cross sections.

From the parton initial state singularities, we deduce

$$
\begin{aligned}
\frac{\mathrm{d}\tilde{\sigma}}{\mathrm{d}t}(\gamma q \rightarrow p_1 p_2) & = \frac{\alpha_s^2(\mu^2)}{2\pi} CT_q \\
& \left\{ \int_{X_b}^1 \frac{\mathrm{d}z_b}{z_b} X_b F_{q/p}\left(\frac{X_b}{z_b}, M_b^2\right) \left[C_F \tilde{J}_1(z_b) + P_{q\leftarrow q}(z_b) \ln \frac{s}{M_b^2} \right] \right. \\
& \left. + \int_{X_b}^1 \frac{\mathrm{d}z_b}{z_b} X_b F_{g/p}\left(\frac{X_b}{z_b}, M_b^2\right) \left[P_{q\leftarrow g}(z_b) \left(\ln\left(\frac{(1-z_b)y_J s}{z_b M_b^2}\right) - 1 \right) + \frac{1}{2} \right] \right\},
\end{aligned}
\tag{80}
$$

$$
\begin{aligned}
\frac{\mathrm{d}\tilde{\sigma}}{\mathrm{d}t}(\gamma g \rightarrow p_1 p_2) & = \frac{3}{8} \frac{\alpha_s^2(\mu^2)}{2\pi} CT_g \\
& \left\{ \int_{X_b}^1 \frac{\mathrm{d}z_b}{z_b} X_b F_{g/p}\left(\frac{X_b}{z_b}, M_b^2\right) \left[-\frac{N_C}{2} \tilde{J}_6(z_b) + P_{g\leftarrow g}(z_b) \ln \frac{s}{M_b^2} \right] \right. \\
& + \int_{X_b}^1 \frac{\mathrm{d}z_b}{z_b} X_b F_{q/p}\left(\frac{X_b}{z_b}, M_b^2\right) \left[P_{g\leftarrow q}(z_b) \left(\ln\left(\frac{(1-z_b)y_J s}{z_b M_b^2}\right) + 1 \right) \right. \\
& \left. \left. -2C_F \frac{1-z_b}{z_b} \right] \right\}.
\end{aligned}
\tag{81}
$$

The functions $\tilde{J}_i$ are the regular parts of the functions J_i defined in appendix D. They contain the cut-off y_J and are distributions in z_b. The dominant terms for $y_J \rightarrow 0$ are again proportional to $(\ln^2 y_J)$ and are related to the soft divergence in the parton initial state. J_2 does not contribute after the appropriate crossing of $(t \leftrightarrow u)$.

The results in (70)-(81) are equivalent to those of Baer et al. [7]. They cannot be compared since these authors introduce a different cut for integrating over the soft singularities. Instead of invariant masses, they use a cut on the energy of the gluon. Terms that are independent of soft singularities agree. For example, this is the case for the cross section in (79) coming from the collinear photon initial state singularity.

4   Inclusive One- and Two-Jet Cross Sections

In this section, we present some characteristic numerical results for one- and two-jet cross sections which have been obtained with our method of slicing the phase space with invariant mass cuts. In a short communication we have used this method to calculate the differential two-jet cross section as a function of average rapidity $\bar{\eta} = \frac{1}{2}(\eta_1 + \eta_2)$ of the two jets of highest transverse energy with the cut on $|\eta_1 - \eta_2| < 0.5$ [20] and compared it to recent experimental data of the ZEUS collaboration at HERA [22]. For this paper, we have calculated various one- and two-jet distributions without applying special cuts on kinematical variables of the initial or final states dictated by the experimental analysis, although our approach is particularly suitable for this

as has been shown in [20].

The input for our calculations is listed in the following. We have chosen the CTEQ3M proton structure function [21], which is a NLO parametrization with $\overline{\text{MS}}$ factorization and $\Lambda^{(4)} = 239$ MeV. This Λ value is also used to calculate the two-loop α_s value at the scale $\mu = E_T$. The factorization scale is also $M = E_T$. We do not apply a special cut on the photon energy fraction x_a in (2) but integrate from $x_{a,\text{min}}$ to 1. $Q^2_{\text{max}} = 4$ GeV^2 is the same as used in the jet analysis of the ZEUS experiment [22].

The further calculation is based on two separate contributions – a set of two-body contributions and a set of three-body contributions. Each set is completely finite, as all singularities have been cancelled or absorbed into structure functions. Each part depends separately on the cut-off y. If y is chosen large enough, the two parts determine physically well defined two-jet and three-jet cross sections. Our analytic calculations are valid only for very small y, since terms $\text{O}(y)$ have been neglected in the analytic integrations. For very small y, the two pieces have no physical meaning. In this case, the $(\ln y)$ terms force the two-body contributions to become negative, whereas the three-body cross sections are large and positive. In [20], we have plotted such cross sections for $y = 10^{-3}$. However, when the two- and three-body contributions are superimposed to yield a suitable inclusive cross section, as for example the inclusive single-jet cross section, the dependence on the cut-off y will cancel. Then, the separation of the two contributions with the cut-off y is only a technical device. The cut-off only serves to distinguish the phase space regions, where the integrations are done analytically, from those where they are done numerically. Furthermore, y must be chosen sufficiently small so that experimental cuts imposed on kinematical variables do not interfere with the cancellation of the y dependence.

First, we consider the inclusive single-jet cross section. To achieve this, we must choose a jet definition, which recombines two nearly collinear partons. As usual, we adopt the jet definition of the Snowmass meeting [23]. According to this definition, two partons i and j are recombined if $R_{i,j} < R$, where $R_i = \sqrt{(\eta_i - \eta_J)^2 + (\phi_i - \phi_J)^2}$ and η_J, ϕ_J are the rapidity and the azimuthal angle of the recombined jet. We choose $R = 1$ in all of the following results. This means that two partons are considered as two separate jets or as a single jet depending whether they lie outside or inside the cone with radius R around the jet momentum. In some cases, it may occur that two partons i and j qualify both as two individual jets i and j and as a combined jet ij. In this case, we make no further selection as it is done in [24], where only the combined jet is counted. In NLO, the final state may consist of two or three jets. The three-jet sample consists of all three-body contributions, which do not fulfill the cone condition.

In Fig. 5, the results for the inclusive one-jet cross section $\text{d}^2\sigma/\text{d}E_T\text{d}\eta$ are shown for various rapidities $\eta = 0, 1$, and 2 as a function of E_T. The NLO and the LO predictions are plotted. The LO curve is calculated with the same proton structure function and the same α_s as the NLO curve. Only the hard scattering cross section is calculated in LO. For $R = 1$, these two cross sections differ only very little. Of course, the NLO cross section depends on R, whereas the LO curve does not. To separate the curves for the three η values, the result for $\eta = 0$ ($\eta = 2$) has been multiplied by 0.1 (0.5).

The maximum of the one-jet cross section is near $\eta = 1$. For $E_T = 20$ GeV, this can be seen from Fig. 6, where $\text{d}^2\sigma/\text{d}E_T\text{d}\eta$ is plotted as a function of η between $\eta = -1$ and $\eta \simeq 4.2$. At this
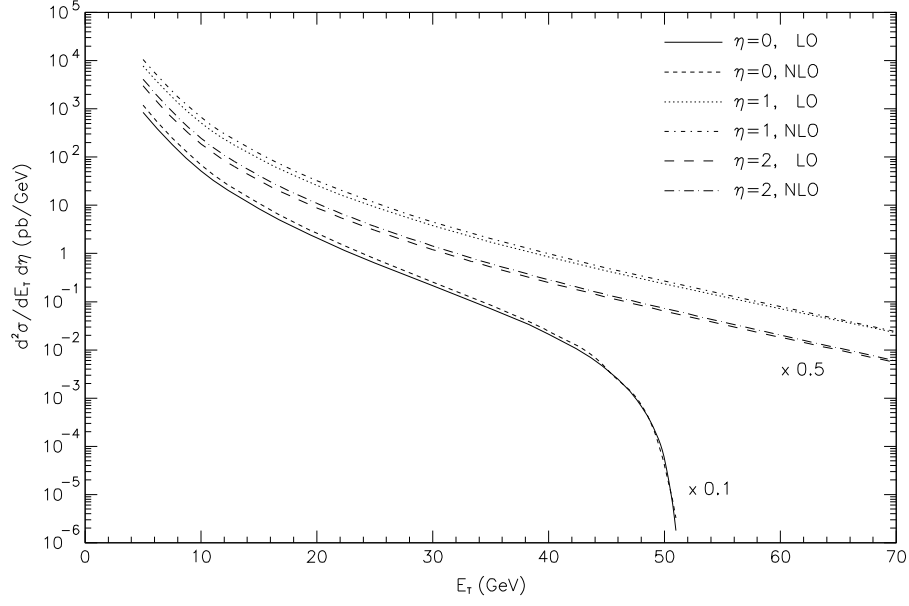
Figure 5: Inclusive single-jet cross section $\mathrm{d}^2\sigma/\mathrm{d}E_T\mathrm{d}\eta$ as a function of E_T for various rapidities $\eta = 0, 1, 2$ in LO and NLO. The cross section for $\eta = 0$ ($\eta = 2$) is multiplied by 0.1 (0.5).
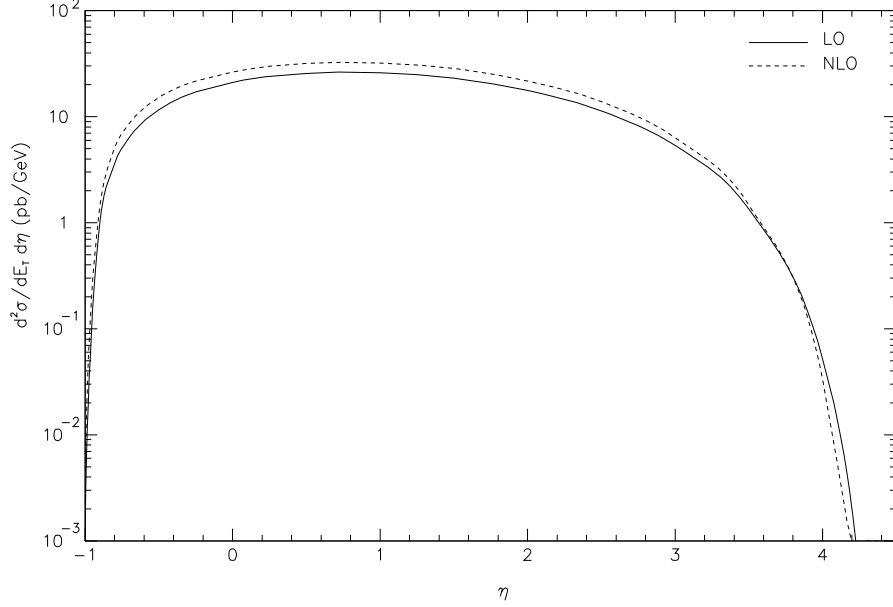

Figure 6: Inclusive single-jet cross section $\mathrm{d}^2\sigma/\mathrm{d}E_T\mathrm{d}\eta$ as a function of η for $E_T = 20$ GeV in LO and NLO.

value of E_T, the kinematical boundaries, where the cross section goes to zero, differ only little in LO and NLO. The k-factor for the NLO prediction is $k \simeq 1.2$ for the central region of $0 \leq \eta \leq 3$.

Our single-jet distributions have been compared with the earlier results of Bödeker [9], who used the subtraction method to cancel soft and collinear singularities. We found perfect agreement. To achieve this, we had to use a rather small value of $y = 10^{-3}$. Furthermore, we had to add some finite contributions of O(1) for $y \to 0$, which correspond to two-jet contributions where an outgoing parton is collinear to another outgoing or an ingoing parton without the corresponding pole term in the $2 \to 3$ matrix elements after partial fractioning. We also checked that our results are independent of y, if y is sufficiently small.

The more essential results are on inclusive two-jet cross sections shown in the following figures. In Fig. 7, we present $\mathrm{d}^3\sigma/\mathrm{d}E_{T_1}\mathrm{d}\eta_1\mathrm{d}\eta_2$ as a function of E_{T_1} for $\eta_1 = 1$ and various choices of $\eta_2 = 0, 1, 2$. Here, E_{T_1} and η_1 are the transverse energy and the rapidity of the so-called trigger jet. η_2 is the rapidity of the second jet, so that E_{T_1} and E_{T_2} are the jets with the highest transverse momenta for the three-jet contribution. For exactly two jets in the final state, we have $E_{T_1} = E_{T_2}$. In Fig. 7, we can see how the cross section decreases when η_2 is chosen away from the maximum region at $\eta_2 = 1$. $\eta_1 = 1$ is always kept fixed. To disentangle the three curves, we have multiplied the $\eta_2 = 2$ ($\eta_2 = 0$) cross section by a factor of 0.5 (0.1) as in Fig. 5. The LO and NLO predictions are very much parallel. The k-factor is $k \simeq 1.2$, similar as in the one-jet cross section. The only large difference between the LO and NLO cross sections occurs at the boundary of the phase space. For example, the cross section for $\eta_2 = 0$ has an additional tail in the E_{T_1} distribution coming from the three-jet cross section, where all three partons lie outside the cone with radius $R = 1$. Such plots can be produced also for other choices of η_1 outside the region where the cross section is maximal.

We have studied the inclusive two-jet cross section also as a function of η_1 and η_2 for fixed E_{T_1}. As an example, we show in Fig. 8 the two-dimensional distribution $\mathrm{d}^3\sigma/\mathrm{d}E_{T_1}\mathrm{d}\eta_1\mathrm{d}\eta_2$ for $E_{T_1} = 20$ GeV in form of a lego-plot in the intervals $\eta_1, \eta_2 \in [-1, 4]$. Over the whole range of η_1 and η_2, the cross section is approximately symmetric in η_1 and η_2. We show this cross section in LO and NLO, and we see clear differences between the LO and the NLO prediction.

This becomes even clearer when we plot the projections for fixed η_1 as a function of η_2. In Fig. 9, these projections are shown for $\eta_1 = 0, 1, 2$, and 3 for LO and NLO. We see that in NLO the cross section is always larger than the LO cross section which is consistent with the k-factor larger than 1 given above.

It is clear that many more distributions or partially integrated cross sections using other two-jet variables can be calculated with the phase space slicing method. As a final application, we have studied the R and the y dependence of the two-jet cross section, integrated over η_1, η_2 and E_{T_1} with a minimal $E_{T_1,\mathrm{min}} = 10$ GeV. The result is shown in Fig. 10, where the LO cross section is independent of R. The NLO cross section is the sum of positive three-body contributions and negative two-body contributions, both calculated with the invariant mass cut $y = 10^{-3}$, and this is not independent of R. However, the dependence is rather weak. The cross section increases with increasing R from $R = 0.1$ to $R = 1$ by a factor of 2 and lies above the LO result for $R \geq 0.6$. For $R < 0.1$, the y cut becomes effective. Therefore we have plotted the curves only for $R \geq 0.1$. The sum of the two-body and three-body contributions depends
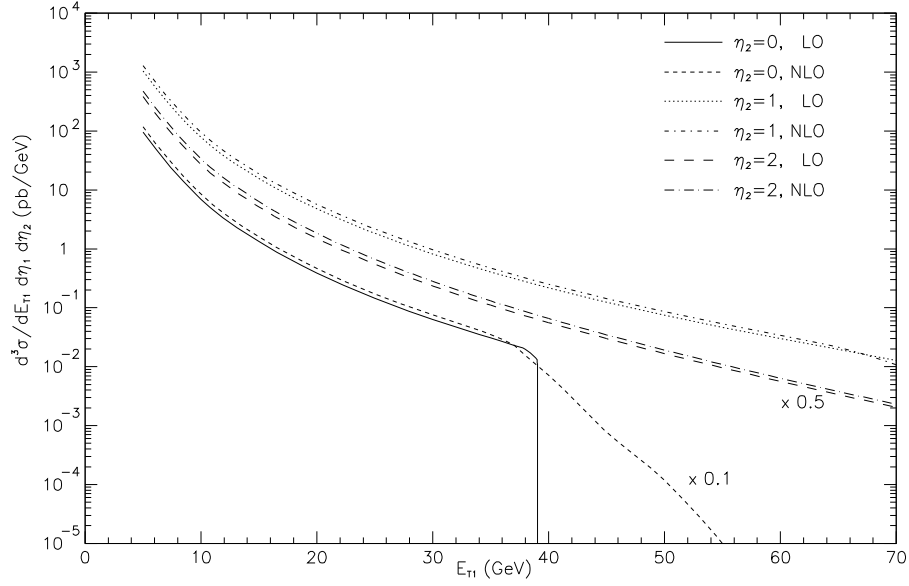
Figure 7: Inclusive dijet cross section $\mathrm{d}^3\sigma/\mathrm{d}E_{T_1}\mathrm{d}\eta_1\mathrm{d}\eta_2$ as a function of E_{T_1} for $\eta_1 = 1$ and three values of $\eta_2 = 0, 1, 2$. The cross section for $\eta_2 = 0$ ($\eta_2 = 2$) is multiplied by 0.1 (0.5).
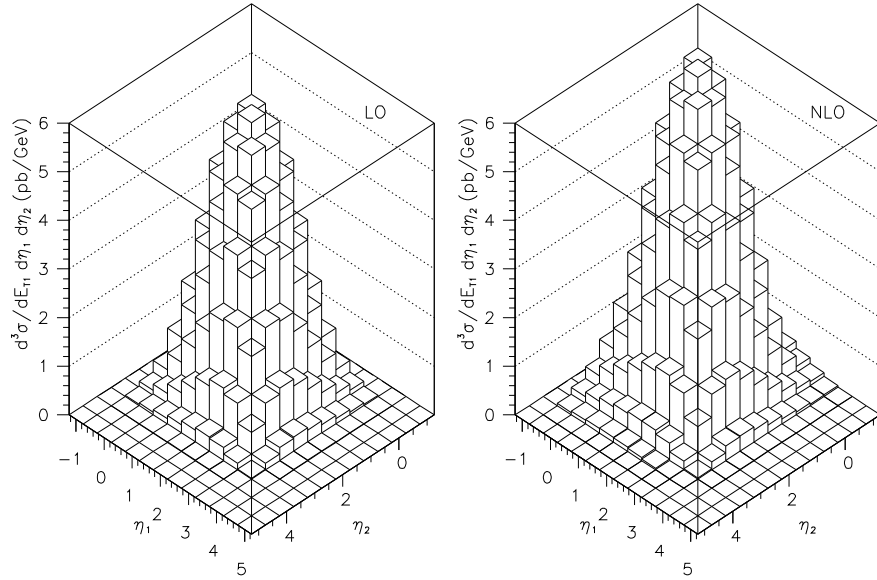

Figure 8: The LO and NLO triple differential inclusive dijet cross section for $E_{T_1} = 20$ GeV as a function of η_1 and η_2.
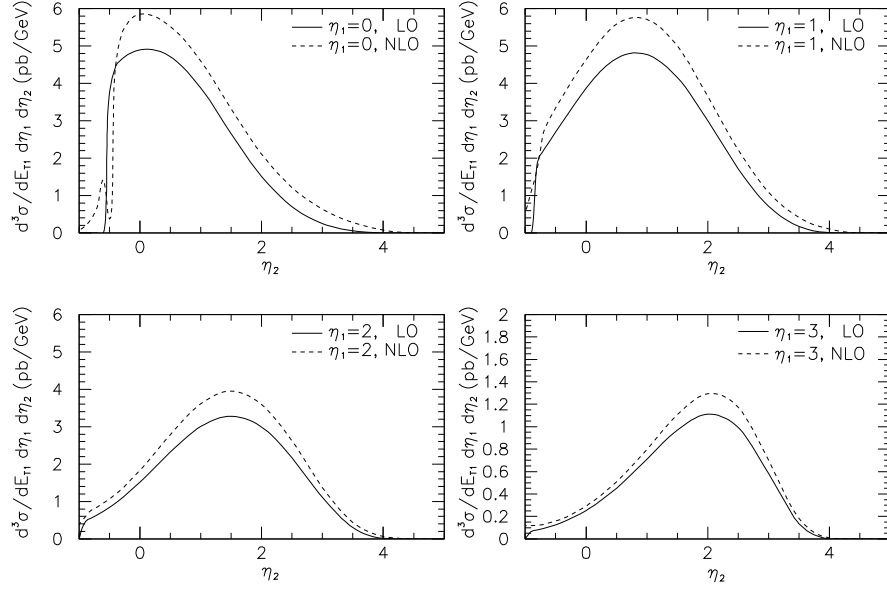
Figure 9: Projections of the LO and NLO triple differential inclusive dijet cross section for $E_{T_1} = 20$ GeV as a function of η_2 for fixed $\eta_1 = 0, 1, 2,$ and 3.

on R like $a + b \ln R + c R^2$ due to the recombination of two parton momenta p_i and p_j inside the cone with radius R. This way, the singled out transverse energy of a jet can differ from the individual parton E_T's. This R dependence has been studied before for the inclusive one-jet cross section with similar results [8, 9].

We have also calculated the same cross section as a function of the invariant mass cut y without the cone recombination. In this case, the cut y operates as a physical cut. Of course, the results for the two-body contributions (being negative for $y < 3 \cdot 10^{-2}$) and the three-body contributions (being above the sum for $y < 3 \cdot 10^{-2}$) only make sense for sufficiently large values of the y cut. For $y \to 0$, the two-body (three-body) contributions decrease (increase) like $-\ln^2 y$ ($\ln^2 y$). The results are presented in Fig. 11. Here we see that the sum of both contributions depends only moderately on y ($\propto \ln y$) due to the recombination of partons in the final state. This dependence on y of the summed contribution is equivalent to the R dependence of the integrated cross section shown in Fig. 10. We remark that in Fig. 11 the respective cross sections must still be corrected by finite terms of O(y). The two-body contribution is calculated from the analytical formulas given above, where these terms are neglected. This should influence our results only for $y > 2 \cdot 10^{-2}$. It is, however, no problem to calculate these terms numerically.
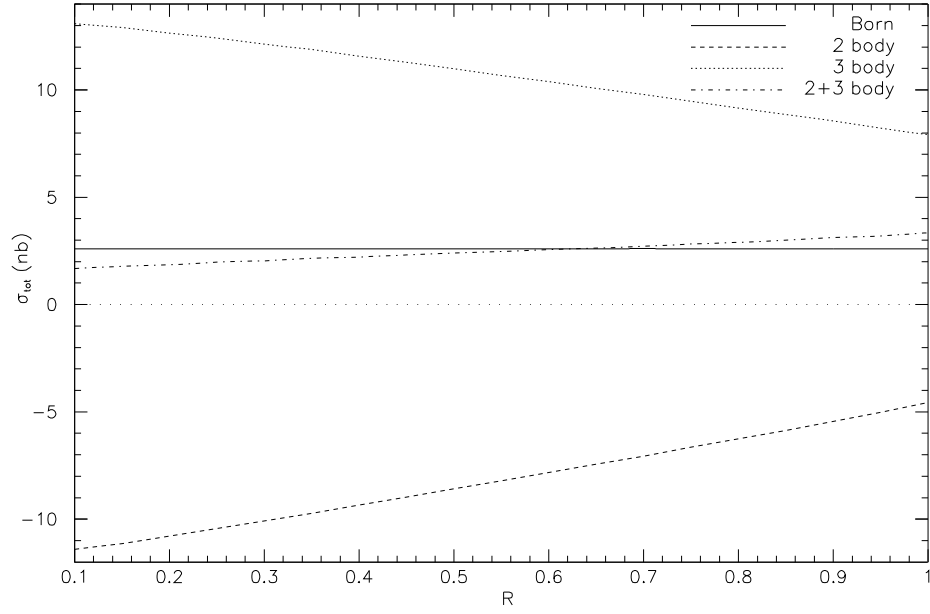
Figure 10: Integrated inclusive dijet cross section for $E_{T_1,\min} = 10$ GeV as a function of R in NLO (dashed-dotted) and LO (full). The 2 body (dashed) and 3 body (dotted) contributions with $y = 10^{-3}$ are plotted separately.
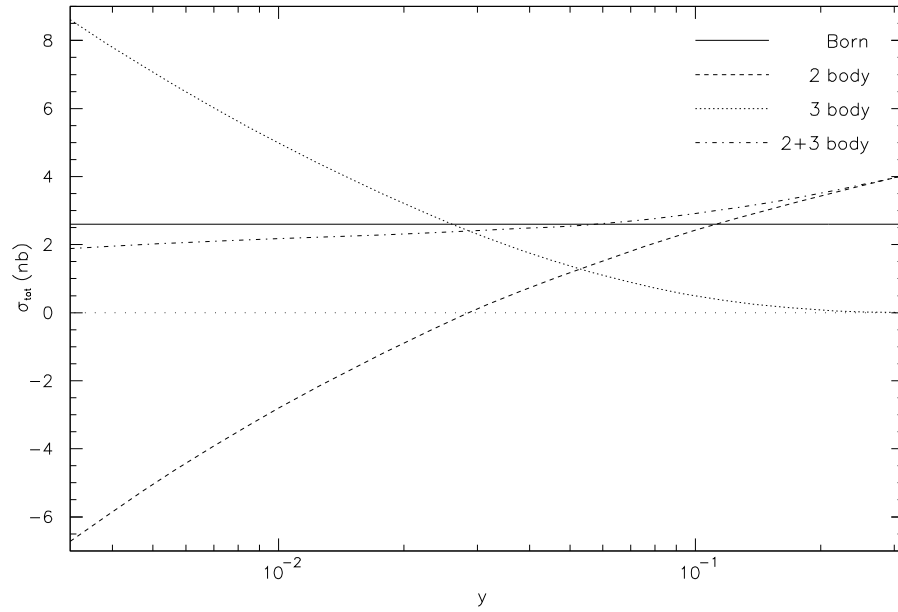

Figure 11: Integrated inclusive dijet cross section for $E_{T_1,\min} = 10$ GeV as a function of y in NLO (dashed-dotted) and LO (full). The 2 body (dashed) and 3 body (dotted) contributions are plotted separately.

5 Summary

Differential cross sections $\mathrm{d}^3\sigma/\mathrm{d}E_T^2\mathrm{d}\eta_1\mathrm{d}\eta_2$ have been calculated in NLO for direct photoproduction. Infrared and collinear singularities are cancelled with the phase space slicing method using an invariant mass cut-off. This method allows to incorporate various cuts on the final state dictated by the analysis of experimental data and to perform calculations for different choices of jet algorithms. Analytical formulas for the different contributions giving the dependence on the slicing parameter are derived. This is needed if one wants to develop a complete description of photoproduction events including hadronization and other corrections. Numerical results for the two-jet inclusive cross sections at HERA have been presented, and LO and NLO predictions have been compared. For a cone radius of $R = 1$, the NLO corrections lead to an increase of the order of 20% compared to the LO prediction which is calculated with the same proton structure function and the same α_s as the NLO prediction.

A Virtual Corrections

In this appendix, we give the interference terms of the virtual corrections with the LO QCD Compton scattering $\gamma q \to gq$ ($= T_q(s,t,u)$) and the LO photon-gluon fusion $\gamma g \to q\bar{q}$ ($= T_g(s,t,u)$) matrix elements as defined in equations (16) and (17). The results depend only on the Mandelstam variables s, t, and u:

$$V_{q1} = \left[-\frac{2}{\epsilon^2} + \frac{1}{\epsilon}\left(2\ln\frac{-t}{s} - 3 \right) + \frac{2\pi^2}{3} - 7 + \ln^2\frac{t}{u} \right] T_q(s,t,u) \tag{A.1}$$
$$- 2\ln\frac{-u}{s} + 4\ln\frac{-t}{s} - 3\frac{s}{u}\ln\frac{-u}{s} - \left(2+\frac{u}{s}\right)\left(\pi^2 + \ln^2\frac{t}{u}\right) - \left(2+\frac{s}{u}\right)\ln^2\frac{-t}{s},$$

$$V_{q2} = \left[\frac{2}{\epsilon^2} + \frac{1}{\epsilon}\left(2\ln\frac{-t}{s} - 2\ln\frac{-u}{s} \right) + \frac{\pi^2}{3} + \ln^2\frac{t}{u} \right] T_q(s,t,u) \tag{A.2}$$
$$- 2\ln\frac{-u}{s} + 4\ln\frac{-t}{s} - \left(2+\frac{u}{s}\right)\left(\pi^2 + \ln^2\frac{t}{u}\right) - \left(2+\frac{s}{u}\right)\ln^2\frac{-t}{s},$$

$$V_{g1} = \left[-\frac{2}{\epsilon^2} - \frac{3}{\epsilon} + \frac{2\pi^2}{3} - 7 + \ln^2\frac{-t}{s} + \ln^2\frac{-u}{s} \right] T_g(s,t,u) \tag{A.3}$$
$$+ 2\ln\frac{-t}{s} + 2\ln\frac{-u}{s} + 3\frac{u}{t}\ln\frac{-t}{s} + 3\frac{t}{u}\ln\frac{-u}{s} + \left(2+\frac{u}{t}\right)\ln^2\frac{-u}{s} + \left(2+\frac{t}{u}\right)\ln^2\frac{-t}{s},$$

$$V_{g2} = \left[\frac{2}{\epsilon^2} + \frac{1}{\epsilon}\left(-2\ln\frac{-t}{s} - 2\ln\frac{-u}{s} \right) + \frac{\pi^2}{3} + \ln^2\frac{tu}{s^2} \right] T_g(s,t,u) \tag{A.4}$$
$$+ 2\ln\frac{-t}{s} + 2\ln\frac{-u}{s} + \left(2+\frac{u}{t}\right)\ln^2\frac{-u}{s} + \left(2+\frac{t}{u}\right)\ln^2\frac{-t}{s}.$$

B Final State Corrections

This appendix contains the real corrections coming from the integration of the $2 \to 3$ matrix elements over the final state singular region of phase space. In addition to the Mandelstam variables, the result depends on the integration cut-off y_F:

$$F_1 = \left[\frac{1}{\epsilon^2} + \frac{1}{\epsilon}\left(-\ln\frac{-t}{s} + \frac{3}{2} \right) - \frac{1}{2}\ln^2\frac{-t}{s} + 2\ln y_F \ln\frac{-t}{s} - 2\mathrm{Li}_2\left(\frac{y_F s}{t}\right) - \frac{\pi^2}{3} + \frac{7}{2} \right. \tag{B.1}$$
$$\left. - \ln^2 y_F - \frac{3}{2}\ln y_F \right] C_F^2 T_q(s,t,u),$$

$$F_2 = \left[-\frac{1}{\epsilon}\ln\frac{-t}{s} - \frac{1}{2}\ln^2\frac{-t}{s} + 2\ln y_F \ln\frac{-t}{s} - 2\mathrm{Li}_2\left(\frac{y_F s}{t}\right) \right]\left(-\frac{1}{2}N_C C_F \right) T_q(s,t,u), \tag{B.2}$$

$$F_3 = \left[-\frac{2}{\epsilon^2} + \frac{1}{\epsilon}\left(\ln\frac{-u}{s} - 2 \right) - 4 + 2\ln y_F + \ln^2 y_F + \ln^2\frac{y_F s}{-u} - \frac{1}{2}\ln^2\frac{-u}{s} + \frac{2\pi^2}{3} \right. \tag{B.3}$$
$$\left. + 2\mathrm{Li}_2\left(\frac{y_F s}{u}\right) \right]\left(-\frac{1}{2}N_C C_F \right) T_q(s,t,u),$$

$$F_4 = \left[-\frac{5}{3\epsilon} + \frac{5}{3}\ln y_F - \frac{31}{9} \right]\left(-\frac{1}{2}N_C C_F \right) T_q(s,t,u), \tag{B.4}$$

25

$$F_5 = \left[-\frac{1}{3\epsilon} - \frac{5}{9} + \frac{1}{3}\ln y_F\right] C_F T_q(s,t,u), \tag{B.5}$$

$$F_6 = \left[\frac{2}{\epsilon^2} + \frac{3}{\epsilon} - \frac{2\pi^2}{3} + 7 - 2\ln^2 y_F - 3\ln y_F\right] \frac{C_F}{2} T_g(s,t,u), \tag{B.6}$$

$$F_7 = \left[\frac{1}{\epsilon}\ln\frac{tu}{s^2} + \ln^2\frac{y_F s}{-t} + \ln^2\frac{y_F s}{-u} - 2\ln^2 y_F - \frac{1}{2}\ln^2\frac{-t}{s} - \frac{1}{2}\ln^2\frac{-u}{s} + 2\mathrm{Li}_2\left(\frac{y_F s}{t}\right) \right. \tag{B.7}$$
$$\left. + 2\mathrm{Li}_2\left(\frac{y_F s}{u}\right)\right]\left(-\frac{N_C}{4}\right) T_g(s,t,u).$$

C Photon Initial State Corrections

Like gluons, real photons can split into $q\bar{q}$ pairs. After integration over the collinear region of phase space, the Born matrix elements for $q\bar{q} \to gg$ $(= T_{1a,b}(s,t,u))$, $qq' \to qq'$ $(= T_2(s,t,u))$, and $qq \to qq$ $(= T_{2,3}(s,t,u))$ can be factorized out. The result depends on the Mandelstam variables, on the integration cut-off y_I, and on the integration variable z_a:

$$I_1 = \left[-\frac{1}{\epsilon}\frac{1}{2N_C}P_{q_i\leftarrow\gamma}(z_a) + \frac{1}{2N_C}P_{q_i\leftarrow\gamma}(z_a)\ln\left(\frac{1-z_a}{z_a}y_I\right) + \frac{Q_i^2}{2}\right] 2C_F^2 T_{1a}(s,t,u), \tag{C.1}$$

$$I_2 = \left[-\frac{1}{\epsilon}\frac{1}{2N_C}P_{q_i\leftarrow\gamma}(z_a) + \frac{1}{2N_C}P_{q_i\leftarrow\gamma}(z_a)\ln\left(\frac{1-z_a}{z_a}y_I\right) + \frac{Q_i^2}{2}\right] (-N_C C_F)T_{1b}(s,t,u) \tag{C.2}$$

$$I_3 = \left[-\frac{1}{\epsilon}\frac{1}{2N_C}P_{q_i\leftarrow\gamma}(z_a) + \frac{1}{2N_C}P_{q_i\leftarrow\gamma}(z_a)\ln\left(\frac{1-z_a}{z_a}y_I\right) + \frac{Q_i^2}{2}\right] 2C_F T_2(s,t,u), \tag{C.3}$$

$$I_4 = \left[-\frac{1}{\epsilon}\frac{1}{2N_C}P_{q_i\leftarrow\gamma}(z_a) + \frac{1}{2N_C}P_{q_i\leftarrow\gamma}(z_a)\ln\left(\frac{1-z_a}{z_a}y_I\right) + \frac{Q_i^2}{2}\right] 2C_F T_2(t,s,u), \tag{C.4}$$

$$I_5 = \left[-\frac{1}{\epsilon}\frac{1}{2N_C}P_{q_i\leftarrow\gamma}(z_a) + \frac{1}{2N_C}P_{q_i\leftarrow\gamma}(z_a)\ln\left(\frac{1-z_a}{z_a}y_I\right) + \frac{Q_i^2}{2}\right] 2\frac{C_F}{N_C}T_3(s,t,u) \tag{C.5}$$
$$+ \text{zycl. permutations of s,t, and u,}$$

$$I_6 = \left[-\frac{1}{\epsilon}\frac{1}{2N_C}P_{q_i\leftarrow\gamma}(z_a) + \frac{1}{2N_C}P_{q_i\leftarrow\gamma}(z_a)\ln\left(\frac{1-z_a}{z_a}y_I\right) + \frac{Q_i^2}{2}\right] (-2C_F)T_{1a}(t,s,u) \tag{C.6}$$
$$+ (t \leftrightarrow u),$$

$$I_7 = \left[-\frac{1}{\epsilon}\frac{1}{2N_C}P_{q_i\leftarrow\gamma}(z_a) + \frac{1}{2N_C}P_{q_i\leftarrow\gamma}(z_a)\ln\left(\frac{1-z_a}{z_a}y_I\right) + \frac{Q_i^2}{2}\right] N_C T_{1b}(t,s,u) \tag{C.7}$$
$$+ (t \leftrightarrow u).$$

The Altarelli-Parisi splitting function $P_{q_i\leftarrow\gamma}$ is equal to $2N_C Q_i^2 P_{q\leftarrow g}$ (see Appendix D).

D Parton Initial State Corrections

In this appendix, the parton initial state corrections are given as a function of the Mandelstam variables s, t, u, of the cut-off y_J, and of the additional integration variable z_b:

$$J_1 = \left[-\frac{1}{\epsilon}\frac{1}{C_F}P_{q\leftarrow q}(z_b) + \delta(1-z_b)\left(\frac{1}{\epsilon^2} + \frac{1}{\epsilon}\left(-\ln\frac{-t}{s} + \frac{3}{2}\right) + \frac{1}{2}\ln^2\frac{-t}{s} + \pi^2\right)\right] \tag{D.1}$$

$$+ 1 - z_b + (1 - z_b) \ln\left(\frac{1 - z_b}{z_b} y_J\right) + 2R_+\left(\frac{-t}{s}\right) - 2\ln\left(\frac{-t}{s}\left(\frac{1 - z_b}{z_b}\right)^2\right)$$

$$\left. - 2\frac{z_b}{1 - z_b}\ln\left(1 + \frac{-t}{y_J s}\frac{1 - z_b}{z_b}\right)\right] C_F^2 T_q(s, t, u),$$

$$J_2 = \left[\delta(1 - z_b)\left(\frac{1}{\epsilon}\ln\frac{u}{t} + \frac{1}{2}\ln^2\frac{-t}{s} - \frac{1}{2}\ln^2\frac{-u}{s}\right) + 2R_+\left(\frac{-t}{s}\right) - 2R_+\left(\frac{-u}{s}\right)\right. \quad \text{(D.2)}$$

$$- 2\ln\left(\frac{-t}{s}\left(\frac{1 - z_b}{z_b}\right)^2\right) + 2\ln\left(\frac{-u}{s}\left(\frac{1 - z_b}{z_b}\right)^2\right)$$

$$\left. - 2\frac{z_b}{1 - z_b}\ln\left(1 + \frac{-t}{y_J s}\frac{1 - z_b}{z_b}\right) + 2\frac{z_b}{1 - z_b}\ln\left(1 + \frac{-u}{y_J s}\frac{1 - z_b}{z_b}\right)\right]$$

$$\left(-\frac{1}{2}N_C C_F\right) T_q(s, t, u),$$

$$J_3 = \left[-\frac{1}{\epsilon}\frac{1}{C_F}P_{g \leftarrow q}(z_b) + \frac{1}{C_F}P_{g \leftarrow q}(z_b)\ln\left(\frac{1 - z_b}{z_b} y_J\right) - 2\frac{1 - z_b}{z_b}\right]\frac{C_F}{2}T_g(s, t, u), \quad \text{(D.3)}$$

$$J_4 = \left[-\frac{2}{\epsilon}P_{q \leftarrow g}(z_b) + 2P_{q \leftarrow g}(z_b)\ln\left(\frac{1 - z_b}{z_b} y_J\right) + 1\right] C_F T_q(s, t, u), \quad \text{(D.4)}$$

$$J_5 = \mathrm{O}(\epsilon), \quad \text{(D.5)}$$

$$J_6 = \left[\frac{2}{\epsilon}\frac{1}{N_C}P_{g \leftarrow g}(z_b) + \delta(1 - z_b)\left(-\frac{2}{\epsilon^2} + \frac{1}{\epsilon}\left(\ln\frac{tu}{s^2} - \frac{2}{N_C}\left(\frac{11}{6}N_C - \frac{1}{3}N_f\right)\right)\right.\right. \quad \text{(D.6)}$$

$$\left. - \frac{1}{2}\ln^2\frac{-t}{s} - \frac{1}{2}\ln^2\frac{-u}{s} - 2\pi^2\right) - 2R_+\left(\frac{-t}{s}\right) - 2R_+\left(\frac{-u}{s}\right)$$

$$+ 2\ln\left(\frac{-t}{s}\left(\frac{1 - z_b}{z_b}\right)^2\right) + 2\ln\left(\frac{-u}{s}\left(\frac{1 - z_b}{z_b}\right)^2\right)$$

$$+ 2\frac{z_b}{1 - z_b}\ln\left(1 + \frac{-t}{y_J s}\frac{1 - z_b}{z_b}\right) + 2\frac{z_b}{1 - z_b}\ln\left(1 + \frac{-u}{y_J s}\frac{1 - z_b}{z_b}\right)$$

$$\left. - 4\left(\frac{1 - z_b}{z_b} + z_b(1 - z_b)\right)\ln\left(\frac{1 - z_b}{z_b} y_J\right)\right]\left(-\frac{N_C}{4}\right) T_g(s, t, u),$$

where we have introduced

$$R_+(x) = \left(\frac{\ln\left(x\left(\frac{1 - z_b}{z_b}\right)^2\right)}{1 - z_b}\right)_+ \quad \text{(D.7)}$$

for convenience. The Altarelli-Parisi splitting functions are defined as

$$P_{q \leftarrow q}(z_b) = C_F\left[\frac{1 + z_b^2}{(1 - z_b)_+} + \frac{3}{2}\delta(1 - z_b)\right], \quad \text{(D.8)}$$

$$P_{g \leftarrow q}(z_b) = C_F\left[\frac{1 + (1 - z_b)^2}{z_b}\right], \quad \text{(D.9)}$$

$$P_{g \leftarrow g}(z_b) = 2N_C\left[\frac{1}{(1 - z_b)_+} + \frac{1}{z_b} + z_b(1 - z_b) - 2\right] + \left[\frac{11}{6}N_C - \frac{1}{3}N_f\right]\delta(1 - z_b), \quad \text{(D.10)}$$

$$P_{q \leftarrow g}(z_b) = \frac{1}{2}\left[z_b^2 + (1 - z_b)^2\right]. \quad \text{(D.11)}$$

27

As the integration over z_b runs from X_b to 1, the + distributions in this paper are defined as

$$D_+[g] = \int_{X_b}^1 \mathrm{d}z_b D(z_b) g(z_b) - \int_0^1 \mathrm{d}z_b D(z_b) g(1), \tag{D.12}$$

where

$$g(z_b) = \frac{1}{z_b} F_{b'/p}\left(\frac{X_b}{z_b}\right) h(z_b), \tag{D.13}$$

and $h(z_b)$ is a regular function of z_b [25]. This leads to additional terms not given here explicitly when (D.12) is transformed so that both integrals are calculated in the range $[X_b, 1]$.

References

[1] J.F. Owens, Phys. Rev. D21 (1980) 54.

[2] M. Drees, F. Halzen, Phys. Rev. Lett. 61 (1988) 275,
M. Drees, R.M. Godbole, Phys. Rev. D39 (1989) 169.

[3] G. D'Agostini, D. Monaldi, Proc. of the Workshop "Physics at HERA", edited by W. Buchmüller and G. Ingelman, Hamburg, 1991, p. 527,
A. Valkarova, ibid., p. 535.

[4] G. Knies, Proc. of the Workshop "Physics at HERA", edited by W. Buchmüller and G. Ingelman, Hamburg, 1991, p. 543,
A. Valkarova, G. Knies, DESY 94-074 (1994).

[5] M. Derrick et al., ZEUS Collaboration, DESY 95-083 (1995).

[6] P. Aurenche, R. Baier, A. Douiri, M. Fontannaz, D. Schiff, Nucl. Phys. B286 (1987) 553,
B.A. Kniehl, G. Kramer, Z. Phys. C62 (1994) 53.

[7] H. Baer, J. Ohnemus, J.F. Owens, Phys. Rev. D40 (1989) 2844.

[8] L.E. Gordon, J.K. Storrow, Phys. Lett. B291 (1992) 320.

[9] D. Bödeker, Phys. Lett. B292 (1992) 164.

[10] D. Bödeker, Z. Phys. C61 (1994) 277.

[11] D. Graudenz, DESY T-90-01 (1990), Phys. Lett. B256 (1991) 518, Phys. Rev. D49 (1994) 3291.

[12] J.R. Forshaw, R.G. Roberts, Phys. Lett. B319 (1993) 539.

[13] B.L. Combridge, J. Kripfgans, J. Ranft, Phys. Lett. B70 (1977) 234,
R. Cutler, D. Sivers, Phys. Rev. D17 (1978) 196,
J.F. Owens, E. Reya, M. Glück, Phys. Rev. D18 (1978) 1501.

[14] R.K. Ellis, D. Ross, A.E. Terrano, Nucl. Phys. B178 (1981) 421.

[15] K. Fabricius, G. Kramer, G. Schierholz, I. Schmitt, Z. Phys. C11 (1982) 315.

[16] D. Bödeker, Doctoral Thesis, University of Hamburg, 1992.

[17] M. Klasen, Diploma Thesis, University of Würzburg, 1993.

[18] R.K. Ellis, M.A. Furman, H.E. Haber, I. Hinchcliffe, Nucl. Phys. B173 (1980) 397.

[19] D. Bödeker, G. Kramer, S.G. Salesch, Z. Phys. C63 (1994) 471.

[20] M. Klasen, G. Kramer, DESY 95-159.

[21] H.L. Lai et al., CTEQ Collaboration, Phys. Rev. D51 (1995) 4763.

[22] M. Derrick et al., ZEUS Collaboration, Phys. Lett. B348 (1995) 665.

[23] J.E. Huth et al., Proc. of the 1990 DPF Summer Study on High Energy Physics, Snowmass, Colorado, edited by E.L. Berger, World Scientific, Singapore, 1992, p. 134.

[24] S.D. Ellis, Z. Kunszt, D.E. Soper, Phys. Rev. Lett. 62 (1989) 726, Phys. Rev. D40 (1989) 2188, Phys. Rev. Lett. 64 (1990) 2121.

[25] M.A. Furman, Nucl. Phys. B187 (1981) 413.